The Henryk Niewodniczański
INSTITUTE OF NUCLEAR PHYSICS
Polish Academy of Sciences
ul. Radzikowskiego 152, 31–342 Kraków, Poland

www.ifj.edu.pl/publ/hab

Kraków, June 2013

Perturbed Angular Correlation method in materials science

Agnieszka Kulińska

Habilitation Thesis

Published by Institute of Nuclear Physics
Polish Academy of Sciences
Kraków, 2013
Recenzent: dr hab. Marta Wolny-Marszałek, prof. IFJ PAN
ISBN 978-83-63542-08-5

Contents

Preface

The investigation of the properties of condensed matter using experimental nuclear methods is becoming increasingly important. An extremely broad range of techniques is used, including the use of particles, such as positrons and neutrons, ion beams, and the detection of radiation from nuclear decays or nuclear reactions. The hyperfine methods based on the interaction of the nuclear electromagnetic moments of the probe nuclei with the hyperfine fields arising from the electronic charges and spin distributions, can characterize materials at the smallest possible atomic scale. In this work, I will demonstrate the potential of Perturbed Angular Correlation (PAC) method in the fundamental research, as well as its application in the solid state and material physics.

Chapter 2 presents a detailed picture of the application of the PAC method to fundamental research of intermetallic compounds performed in the last decade. I selected the Hf-Al and Zr-Al systems as a model example to illustrate the comprehensive measurements of the electric field gradients (EFG) and their temperature dependencies, and to demonstrate the precision and efficiency of the PAC technique. The comparison of the experimental data with the calculated ones confirmed the high quality of the obtained results. In this Chapter, I discussed the problems of (i) the impurity location in a lattice, (ii) site and phase preference of the probes in selected cases of: $HfAl_3$, $ZrAl_3$, ZrAl and ZrAg, (iii) temperature dependencies of the EFG.

Chapter 3 describes the selected examples of the PAC application in condensed matter and material physics study. From among the numerous possibilities I selected a few cases to illustrate the sensitivity and advantages of this hyperfine method. I discussed the following topics: (i) the impurity influence on the electric field gradient and the magnetic hyperfine field, (ii) the application of the PAC method in the nanocrystalline materials study (Hf-Al and Fe-Mn powders), (iii) oxidation of intermetallic compounds (Zr-Al

compounds annealed in air), (iv) the impurity influence on martensitic phase transformation (TiPd shape memory alloys).

This monograph is based on the published papers, as well as the results that have not been published yet.

1. Introduction

The nuclear solid state methods involve inter alia the detection of the particles or γ–radiation from the nuclear decays or nuclear reactions to investigate the properties of condensed matter. This extremely broad range of methods can be divided into two main groups: ion beam analysis (IBA) and hyperfine interaction (HFI) techniques. The various methods from the first group are very important for determination of the elemental composition of materials, and for atomic arrangement. The widely used and most well-known technique is the Rutherford Backscattering Spectroscopy (RBS), which is based on the elastic backscattering of charged particles by nuclei in solids. Hyperfine techniques such as the Mössbauer spectroscopy (MS), the Nuclear Magnetic Resonance (NMR), and the Perturbed Angular Correlation (PAC) have been extensively employed to investigate the structural, magnetic and electronic properties at atomic scale in the condensed matter [Sch96].

In this work, I present the use of the PAC method in fundamental research of the condensed matter as well as its application in the solid state and material physics. I give the results of the intensive studies on the intermetallic compounds, oxides, magnetic materials; thin films and nanocrystalline materials. I summarize the EFG parameters for Hf-Al and Zr-Al intermetallic systems.

1.1. Perturbed Angular Correlation method (PAC)

The time-differential perturbed angular correlation (TDPAC) method uses nuclei, which decay by emitting a sequence of the γ– rays. The intermediate nuclear state has a sufficiently long lifetime for nuclear spin precession to be observed [Fra65]. The full abbreviation TDPAC is used to emphasize that the method is time-differential PAC; however, in this work the shorter PAC abbreviation will be used for brevity. The observation of the first γ_1–quanta of

a γ_1–γ_2 cascade in a fixed direction selects an aligned sub-ensemble of nuclear spins. The basic requirement of PAC is the anisotropic angular distribution of the second γ_2 quanta. In solids, the nuclear moments of the intermediate state interact with the hyperfine field causing a time dependent redistribution of the population of the *m*-substates, which perturbs the angular distribution of the second γ_2–quantum. Hence, the PAC method can provide useful information on the hyperfine field acting on the probe nuclei.

The probability distribution of finding γ_2 at the certain angle θ with respect to the direction of γ_1 is given by $W(\theta)$, which can be expanded into a series of Legendre polynomials $P_k(\cos\theta)$

$$W(\theta) = \sum_k \mathrm{A_k}(1)\mathrm{A_k}(2)\mathrm{P_k}(\cos\theta), \tag{1.1}$$

where A_k (1) and $A_k(2)$ are the anisotropy coefficients determined by the nuclear properties of the first and second γ transition, respectively [Fra65]. The summation index *k* takes non-negative even integers with the upper limit determined by spins of the nuclear states involved and the multipolarities of the two γ rays. If the direction of the nuclear spin in the intermediate state varies with time, the angular correlation function becomes time dependent ($W(\theta,t)$). In a polycrystalline sample the distribution function can be described with

$$W(\theta,t) = \sum_k A_{kk} G_{kk}(t) P_k(\cos\theta). \tag{1.2}$$

The perturbation factor $G_{kk}(t)$ includes information about the magnetic dipole and/or the electric quadrupole interaction causing the change of the nuclear spin direction. The higher order terms are usually neglected, and the Equation 1.2 in lowest order can be written as

$$W(\theta,t) = 1 + A_{22} G_{22}(t) P_2(\cos\theta). \tag{1.3}$$

As long as the hyperfine interaction is constant during the observation time, the probe nuclei are exposed to the static pure electric interaction, and the perturbation factor $G_{22}(t)$ is given by

$$G_{22}(t) = \sum_{n=0}^{3} s_{2n}(\eta)\cos\left[g_{2n}(\eta)\nu_Q t\right], \tag{1.4}$$

where the hyperfine interaction (*hfi*) parameters are described by the quadrupole coupling constant

$$\nu_Q = eQV_{zz}/h \tag{1.5}$$

and the asymmetry parameter $\eta = (V_{xx}-V_{yy})/V_{zz}$.

The electric field gradient (EFG) acting on a nucleus in the lattice position of the non-cubic arrangement of the nearby atomic cores and electrons causes a splitting of the nuclear levels due to the electric quadrupole interaction between the nuclear quadrupole moment Q and this field gradient. The $g_{2n}(\eta)$ coefficients describe the quadrupole splitting of the intermediate state of the probe nuclei. V_{ii} are the components of the EFG tensor in the principal axes frame. Determination of the *hfi* parameters gives the information about the strength (V_{zz}) and symmetry (η) of the observed electric field gradient. The approximate values for $s_{2n}(\eta)$ and $g_{2n}(\eta)$ given in the form of polynomials of η, calculated using the coefficients for the polycrystalline samples, are tabulated in [Kaj73].

Considering that the probe nuclei situated at the different lattice sites can experience different local EFGs, the experimental data can be least square fitted with

$$G_{22}^{el} = \sum_i f_i \sum_{n=0}^{3} s_{2n}(\eta_i)\cos\left[g_{2n}(\eta_i)\nu_{Qi}t\right]\exp\left[-g_{2n}(\eta_i)\delta_i t\right]\sigma\left(g_{2n}(\eta_i)\nu_{Qi},\tau_R\right). \qquad (1.6)$$

The fraction f_i reflects the occupation of nonequivalent probe sites in the structure of the investigated sample. The imperfections of the crystal lattice structure (defects, impurities, etc.) which occur in the experiment very often lead to damping of the measured perturbation factor, i.e. the distribution of the EFG. This is described by the width δ of the quadrupole frequency distribution of the Lorentzian shape.

In the case of the static magnetic field acting on the probe nuclei, the perturbation factor is fitted with

$$G_{22}^{magn} = \sum_i f_i \sum_{n=0}^{2} s_{2n}\cos\left[n\omega_L t\right]\exp\left[-n\delta_i t\right]\sigma\left(\omega_L,\tau_R\right). \qquad (1.7)$$

The precession frequency of the magnetic moment around the field is given by

$$\omega_L = \mu B_{hf}/\hbar, \qquad (1.8)$$

known as the Larmor frequency. The B_{hf} is the hyperfine magnetic field; μ is the magnetic moment of the intermediate state.

The σ parameter in Equations 1.6 and 1.7 takes into account the finite time resolution of the apparatus τ_R [Ber69]. The coefficients s_{2n} depend on the single– or polycrystalline form of the sample. In the case of textured samples, the s_{2n} amplitudes in Equations 1.6 and 1.7 are treated as free parameters in the fitting procedure.

1.2. Experimental details

The time developments of the angular correlation can be visualized qualitatively as a rotation of the radiation emission pattern. Usually, four detectors based on BaF_2 and/or NaI scintillators at fixed angle θ (90° and 180°) are used for recording the coincident count rates as a function of time between emission of γ_1 and γ_2. The intensity ratio R(t) of the combination of the coincidence time spectra

$$R(t) = 2\frac{N(180°,t)-N(90°,t)}{N(180°,t)+2N(90°,t)} \tag{1.9}$$

directly related to the perturbation factor G_{22}(t) by

$$R(t) = A_{22}^{eff}\sum_i f_i G_{22}^i(t) \tag{1.10}$$

and corrected for the background is obtained in the PAC experiments.

The most important requirement for an application of the PAC technique is the use of radioactive sources that possess an isomeric level with a lifetime of a few nanoseconds up to several microseconds. The time limits are set by the time resolution of the experimental apparatus and by the signal-to-noise considerations (the real coincidence – to accidental coincidence count rate decreases as $1/\tau_N$). In the presented experiments, two most commonly used PAC probes were: i) ^{181}Ta being a product of β^- decay of ^{181}Hf, and ii) ^{111}Cd being a product of electron capture decay of ^{111}In. The intermediate levels of these probe nuclei have the quadrupole moment Q and magnetic dipole moment μ large enough for the electric field gradient and the magnetic field investigations, respectively. The local electronic changes that occur because of the mother isotope's decay have in metals the time scale of 10^{-12} –10^{-13} s– the time scale of electronic relaxation. The PAC measurement is performing during 10^{-8} – 10^{-7} s, so the daughter nucleus can be considered as being in unperturbed electronic environment. The probe mobility, the position in a lattice, the site occupation, etc. are determined by the properties of each mother isotope, but the hyperfine fields are measured for the daughter isotope's excited level.

The typical radioactive source I used had the activity of 0.5-1 MBq, sufficient for the proper counting rate in the PAC measurements. The ^{181}Hf/^{181}Ta probes were produced via neutron irradiation of the natural hafnium in the Maria reactor in Świerk (^{180}Hf(n,γ)^{181}Hf nuclear reaction), whereas the ^{111}In/^{111}Cd were commercially available as a carrier-free $^{111}InCl_3$

solution. Then, the probes were introduced into the investigated samples by various methods (melting, implantation) according both to the type of the sample – bulk, nanopowder, or layer – and to the isotope used. Since the half-life of the ^{181}Hf and ^{111}In isotopes amounts to 42.4 days and 2.83 days, respectively, the sample retains sufficient activity to perform the experiments for 3-4 months or 2-3 weeks, respectively.

The following procedures were applied to prepare different types of sample:

- bulks: a proper amount of the high purity components were arc-melted a few times under argon atmosphere, followed by the annealing at appropriate temperature;
- nanopowders: mechanically grounding under Ar atmosphere of the previously prepared bulk samples using the high-energy ball milling SPEX2000 equipped with the acrylic vial and two tungsten carbide balls;
- layers: e-gun or thermal deposition of a given thickness of the materials on the crystalline Si or the amorphous SiO_2 substrate using the high vacuum evaporation chamber Univex300.

The PAC probes were introduced into the investigated samples via the following methods:

- neutron irradiation of the prepared compounds containing hafnium as one of the components or as an admixture,
- melting of the radioactive source together with the compounds' constituents,
- ion implantation using an ion implanter (only in the case of ^{111}In/^{111}Cd).

Usually, before the PAC experiments, the X-ray diffraction analysis – sensitive to long-range order –was applied to check the crystal structure of the prepared samples. An additional detailed description of the experimental procedure will be presented at the beginning of each section, where necessary. PAC measurements below room temperature were performed using a closed cycle helium refrigerator, while above 300 K a small resistance heater or vacuum oven was applied. The spectra were collected with a standard slow-fast coincidence set-up with four BaF_2 or NaI(Tl) detectors having the time resolution of about 1 ns and 3 ns, respectively, for 133 keV – 482 keV γ–γ cascade in ^{181}Ta.

1.3. Application of the PAC technique

When applying the HFI methods, one measures the hyperfine interaction, i.e. the interaction between the nucleus magnetic dipole or the electric quadrupole moment and the magnetic or electric hyperfine field produced at the nucleus. Because the hyperfine interaction is short-range, it provides information on the local surroundings of particular atoms. The Perturbed Angular Correlation method is one of the HFI methods supplying information about the local electric and chemical environment of the probe nuclei. The PAC technique, very sensitive to changes at the vicinity of the probe atoms, offers unique possibilities for investigation of the structure and dynamics of the nearest neighborhood of the probes, hence it is a perfect tool to study the polymorphic transformation even in its very early stage.

The intermetallic compounds and the solid-state transformations taking place in the binary metallic systems are of a great technical and metallurgical importance, since almost all industrial alloys are heat-treated after the preparation to improve their properties. Because information included in the PAC spectra is derived from the whole specimen volume, it is possible to perform measurements for the alloys of a different stoichiometry and at different temperatures, and the results enable determination of the homogeneity and temperature region of the phase under study.

For a long time a quantitative computation of the electric field gradient has been a very difficult problem. In recent years, this has changed due to the application of all-electron *ab initio* band structure theories, especially by using the full-potential linearized augmented plane wave method (FLAWP) [Bla88, Bla01] within the framework of the Density Functional Theory (DFT) [Hoh64, Koh65]. For a reliable prediction of the EFG, most commonly a supercell approach is used. In this approach a probe atom is located at the center of a supercell large enough to accommodate significant relaxation. The combination of the *ab initio* calculation and PAC experiments can shed light on the impurity localization in the lattice, and the preferential site occupation of the probe atoms.

2. Fundamental research with PAC[1]

2.1. Electric field gradient in the intermetallic compounds

Intermetallic compounds are being considered as an important class of materials for a variety of applications. A special attention has been given to the alloys based on aluminides due to their high melting points, good oxidation resistance and desired mechanical properties. The intermetallic compounds in equilibrium have a well-defined and unique crystal structure. PAC experiments on those compounds contribute to the understanding of the hyperfine field behavior in different metallic systems. Because this method is very sensitive to the microstructure around the probe atoms, it can be used to follow changes on a nanometer scale. Each position of the probe atom relative to the neighboring atoms usually gives its own characteristic and distinguishable signal, providing information about the EFG values at the substitutional lattice sites. In recent years, it has become possible to obtain the EFG from first-principles electronic structure calculations in the framework of the Density Functional Theory (DFT) [Hoh64, Koh65].

Aluminides (Hf-Al and Zr-Al systems)

In the last decade comprehensive studies of Hf and Zr aluminides were performed. Their phase diagrams contain numerous stoichiometric intermetallic phases of very narrow concentration ranges and various hexagonal, orthorhombic, tetragonal and cubic structures. This study is a perfect illustration of the application of the Perturbed Angular Correlation method to investigate intermetallic compounds, and especially to study the

[1] This chapter includes data published in [Kul06, Wod07, Err10, Wod03, Wod04, Wod09] as well as results that have not been published yet. The author contributed in a great deal in all these works.

lattice location of impurity atoms in the polycrystalline materials. PAC experiments were performed using both most common hyperfine probes ^{181}Hf/^{181}Ta and ^{111}In/^{111}Cd. The ^{181}Hf/^{181}Ta probes are constituent atoms in Hf aluminides and can be considered as such in Zr aluminides due to the chemical similarities of Hf and Zr. On the contrary, the ^{111}In/^{111}Cd probe has to be treated as an impurity in those compounds. Since Hf and Zr are isoelectronic, their aluminides show pronounced similarities in their structure, hyperfine interactions, and other properties.

The quadrupole interaction parameters, i.e. the quadrupole frequency ν_Q,

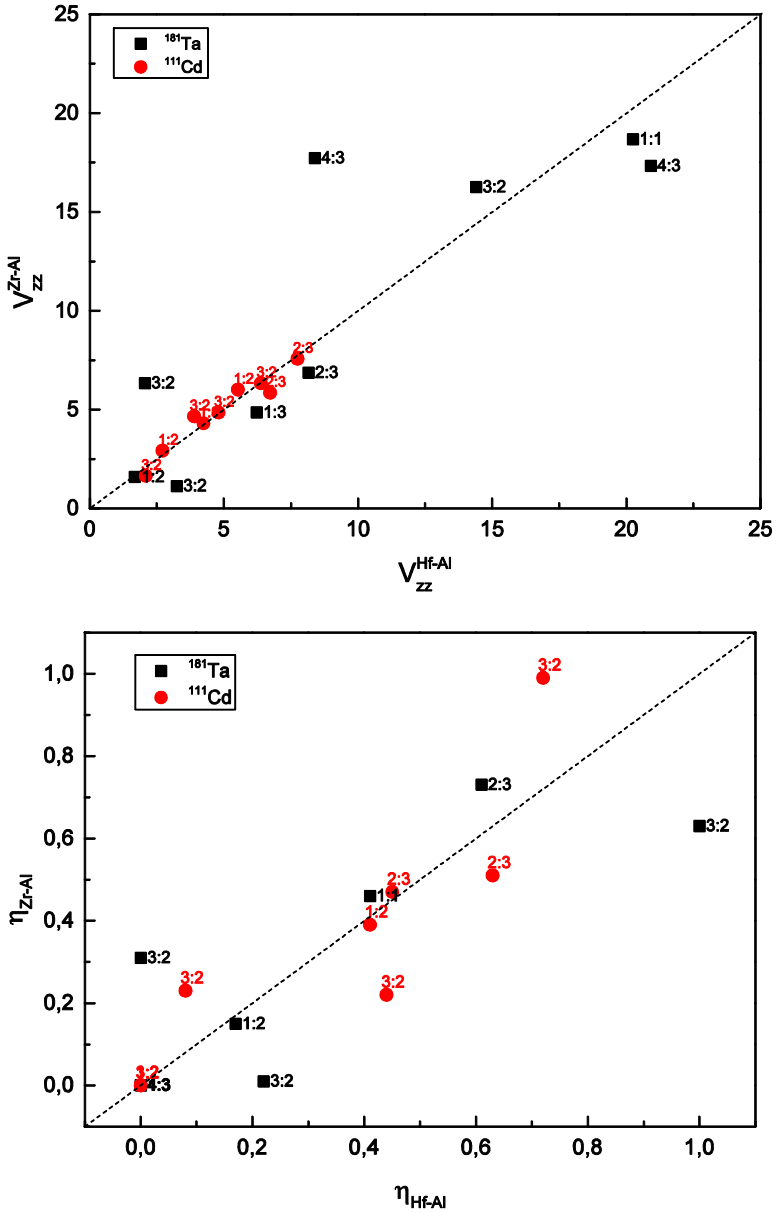

Fig. 2.1 Correlation between V_{zz} values and parameter η measured in Hf- and Zr-aluminides doped with ^{181}Hf/^{181}Ta (black squares) and ^{111}In/^{111}Cd (red circles) probes at room temperature. Numbers indicate the Hf:Al and Zr:Al atomic ratio in the compounds.

the corresponding electric field gradient (values at room temperature and extrapolated to 0 K), the asymmetry parameter η of ^{181}Hf/^{181}Ta and ^{111}In/^{111}Cd probes in Hf-Al and Zr-Al compounds, which we determined in experiments, are collected in Table 2.1 and Table 2.2. The values of the main EFG tensor component $|V_{zz}|$ were deduced from the measured ν_Q according to Equation 1.5 and adopting the quadrupole moment Q of the intermediate level in ^{181}Ta and ^{111}Cd equal to 2.36(5)*b* [Her80] and 0.83(13)*b* [But83], respectively. The uncertainties of the quadrupole moments were not taken into consideration. Hence, the quoted errors are only the instrumental and statistical ones. Values of the EFGs calculated by the other are also included in these Tables. A comparison of the experimental V_{zz}^{exp} and η values obtained at room temperature for both probes at the nonequivalent lattice sites in the corresponding hafnium and zirconium aluminides is shown in Figure 2.1.

The quadruple frequency reaches values from a few tens MHz to above 1 GHz when measured at ^{181}Hf/^{181}Ta and up to ca. 150 MHz when ^{111}In/^{111}Cd probes are used. The PAC spectra for all Hf-Al and Zr-Al compounds exhibit the well-defined axially or non-axially symmetric EFGs corresponding to the particular crystallographic sites occupied by the probes. The V_{zz} values obtained at ^{181}Hf/^{181}Ta in Zr-Al phases are quite similar to those in corresponding Hf-Al phases (Figure 2.1 black square).

The *hfi* parameters obtained for Hf and Zr aluminides doped with ^{111}In/^{111}Cd probes, collected in Table 2.2, are presented in Figure 2.1 (red circles). The V_{zz} values determined for Hf-Al compounds are very close to those of Zr-Al compounds. The relative difference between the $V_{zz}^{Hf\text{-}Al}$(RT) and $V_{zz}^{Zr\text{-}Al}$(RT) measured at ^{111}In/^{111}Cd is much smaller than that measured at ^{181}Hf/^{181}Ta.

The asymmetry parameters η determined for both probes are quite similar for most compounds. If the site occupied by the probe atoms has no axial symmetry some discrepancies are observed; the largest in the Hf_3Al_2 and Zr_3Al_2 compounds. Very close V_{zz} and η values obtained for the most Hf- and Zr- aluminides reflect the chemical and structural similarities of these compounds.

Table 2.1. The experimental and calculated *hfi* parameters of ^{181}Ta in Hf-Al and Zr-Al compounds; V_{zz} in units of 10^{21} V/m^2.

compound	lattice site	ν_Q (RT) [MHz]	V_{zz}^{exp} (RT)	η^{exp}(RT)	$\lvert V_{zz} \rvert^{exp}$ (T=0K)	V_{zz}^{calc}	η^{calc}	Ref. exp	Ref. calc
Zr_3Al	Zr 3c	627(3)	10.99	0	11.72	10.7	0	Wod04	unp
	Al 1a								
Zr_2Al	Zr 2a	1107(4)	19.35	0	19.95			Wod04	
	Zr 2d	43(2)	0.75	0					
	Al 2c								
Hf_3Al_2	Hf 4d	822(1)	14.4	0.22	15.01			Wod05	
	Hf 4f	185(2)	3.24	0	4.27				
	Hf 4g	117(1)	2.05	1	1.90				
	Al 8j								
Zr_3Al_2	Zr 4d	928(3)	16.26	0.01	17.29			Wod05	
	Zr 4f	65(1)	1.13	0.31	0.54				
	Zr 4g	362(2)	6.34	0.63	7.07				
	Al 8j								
Hf_4Al_3	Hf 2d	1193(4)	20.91	0	21.27	20.5	0	Wod07	Wod07
	Hf 2e	479(3)	8.39	0	8.46	9.1	0		
	Al 3f								
Zr_4Al_3	Zr 2d	989(5)	17.33	0	17.8	17.6	0	Wod07	Wod07
	Zr 2e	1012(15)	17.73	0	18.0	18.6	0		
	Al 3f								
HfAl	Hf 4c	1155(3)	20.24	0.41	21.24			Wod03	
	Al 4c								
ZrAl	Zr 4c	1066(1)	18.68	0.46	19.68			Wod03	
	Al 4c								
Hf_2Al_3	Hf 16b	465(1)	8.15	0.61	8.52			Wod00	
	Al 16b							Wod01	
	Al 8a								
Zr_2Al_3	Zr 16b	392(1)	6.87	0.73	7.20			Wod01	
	Al 16b								
	Al 8a								
$HfAl_2$	Hf 4f	96(1)	1.68	0.17	1.57	-1.7	0	Wod02	unp
						-2.3	0		Bel07
	Al 2a								
	Al 6h								
$ZrAl_2$	Zr 4f	90(1)	1.58	0.15	1.50	-1.6	0	Wod02	unp
						-3.2	0		Bel07
	Al 2a								
	Al 6h								
$HfAl_3$ ht	Hf 2a	735(7)	12.9	0.17	12.90*	-12.2	0	Kul10	Kul12
	Al 2b					16.0	0		
	Al 4d					-17.9	0		
$HfAl_3$ lt	Hf 4e	355(2)	6.22	0	6.31	-7.0	0	Wod00	Kul12
	Al 4c					13.3	0,66	Wod01	
	Al 4d					-14.0	0		
	Al 4e					14.6	0		
$ZrAl_3$	Zr 4e	277(1)	4.85	0	5.28	-5.9	0	Wod01	Kul12
	Al 4c					11.3	0		
	Al 4d					-13.2	0		
	Al 4e					14.0	0		

Table 2.2. The experimental and calculated *hfi* parameters of ^{111}Cd in Hf-Al and Zr-Al compounds; V_{zz} in units of 10^{21} V/m^2.

compound	lattice site	ν_Q (RT) [MHz]	V_{zz}^{exp} (RT)	η^{exp}(RT)	$\lvert V_{zz}\rvert^{exp}$ (T=0K)	V_{zz}^{calc}	η^{calc}	Ref. exp	Ref. calc
Zr_3Al	Zr 3c	29(2)	1.44	0	1.32			Wod04	
	Al 1a	0		0					
Zr_2Al	Zr 2a								
	Zr 2d								
	Al 2c	137(2)	6.83	0	7.52			Wod04	
Hf_3Al_2	Hf 4d	78(2)	3.89	0	4.10	-4.2	0	Wod05	Unp
	Hf 4f	42(1)	2.09	0.08	2.2	1.2	0.37		
	Hf 4g	96.3(5)	4.8	0.72	4.97	3.8	0.97		
	Al 8j	128(1)	6.38	0.44	6.5	3.9	0.08		
Zr_3Al_2	Zr 4d	93.6(5)	4.66	0	5.04	-4.4	0	Wod05	unp
	Zr 4f	33(1)	1.64	0.23	1.72	2.2	0.76		
	Zr 4g	97.3(5)	4.85	0.99	5.15	-4.0	0.80		
	Al 8j	127(1)	6.33	0.22	6.67	5.1	0.08		
Hf_4Al_3	Hf 2d					8.78	0	Wod07	Err10
	Hf 2e					-2.46	0		
	Al 3f					5.63	0.91		
Hf_3Al_2	Hf 4d	88(5)	4.4(3)	0	4.3(4)	-3.9	0	Err10	Err10
	Hf 4f	39(2)	1.9(1)	0.12(5)	2.0(2)	1.1	0.17		
	Hf 4g	96.4	4.8	0.74	5.0(1)	4.6	0.62		
	Al 8j	128	6.4	0.44	6.7(1)	6.7	0.1		
Zr_4Al_3	Zr 2d					8.6	0	Wod07	Err10
	Zr 2e					-0.03	0		
	Al 3f	115(2)	5.73(5)	0.21(5)	5.9(1)	5.32	0.82		
Zr_3Al_2	Zr 4d	84(3)	4.2(1)	0.08(5)	4.5(2)	-3.7	0	Err10	Err10
	Zr 4f	34(2)	1.69(5)	0.30(3)	1.7(1)	1.5	0.34		
	Zr 4g	97.7(7)	4.87(3)	0.92(4)	5.1(1)	-4.6	0.85		
	Al 8j	130(1)	6.48(5)	0.30(4)	6.9(1)	6.9	0.26		
HfAl	Hf 4c	128.3(5)	6.38	0.42	6.61			Wod03	
	Al 4c								
ZrAl	Zr 4c								
	Al 4c								
Hf_2Al_3	Hf 16b							Wod00	
	Al 16b	155.3(5)	7.74	0.45	8.02			Wod01	
	Al 8a	135(1)	6.73	0.63	6.99				
Zr_2Al_3	Zr 16b								
	Al 16b	151.9(5)	7.57	0.47	7.88			Wod01	
	Al 8a	117(1)	5.85	0.51	6.06				
$HfAl_2$	Hf 4f	156.5(5)	7.77	0	7.46	-1.7	0	Wod01a	Bel07
	Al 2a	110.9(5)*	5.53	0	5.41	7.2	0	Wod02	
	Al 6h	54.4(5)*	2.71	0.41	2.67	3.7	0.35		
$ZrAl_2$	Zr 4f								
	Al 2a	120.6(5)	6.01	0	5.88	7.1	0	Wod02	Bel07
	Al 6h	58.7(5)	2.93	0.39	2.88	3.9	0.29		
$HfAl_3$ ht	Hf 2a					-2.7	0		Kul12
	Al 2b					10.4	0		
	Al 4d					-6.8	0		
$HfAl_3$ lt	Hf 4e					-1.0	0	Wod00	Kul12
	Al 4c					9.7	0,01	Wod01	
	Al 4d	85.0(5)	4.24	0	4.34	-5.0	0		
	Al 4e					9.7	0		
$ZrAl_3$	Zr 4e					-1.1	0	Wod01	Kul12
	Al 4c					9.7	0,05		
	Al 4d	86.4(5)	4.31	0	4.45	-5.2	0		
	Al 4e					9.3	0		

Correlation between the experimental and calculated EFG

A significant difference between the corresponding EFGs was observed only for the isostructural compounds with 4:3 atomic ratio (42.85 at.% Al). In the Hf_4Al_3 phase two quite distinct EFGs were found in comparison to the very similar EFGs in Zr_4Al_3 phase. Room temperature V_{zz} values (in units of $10^{21}V/m^2$) at the corresponding 2*d* site amount to 20.1(1) and 8.4(1), and at 2*e* site to 17.3(1) and 17.7(3) for hafnium and zirconium aluminides, respectively [Wod07].

In order to better understand the differences in EFGs in these two compounds, the calculations based on the DFT using the full potential augmented plane–wave + local–orbitals (APW+lo) [And75, Mad01, Sjö00] formalism as implemented in the WIEN2k package [Bla01] were done by S. Cottenier and H.M. Petrilli and their coworkers. The calculations were performed with and without the substitutional Ta impurities included in the isostructural Hf_4Al_3 and Zr_4Al_3 compounds [Wod07]. The calculated V_{zz} values at the Zr and Hf replaced by Ta are in a good agreement with the experimental ones shown in Table 2.1. However, in the pure compounds the calculated EFGs values at the Zr and Hf sites turn out to differ a lot from the experimental data. Consequently, the very different EFGs in pure Zr_4Al_3 at the two Zr sites become similar only when dilute Ta impurities replace the Zr atoms. Large changes caused when replacing the Zr lattice atoms by Ta impurity can also be a reason for the difference in the temperature dependence parameters obtained for these two compounds. In the other isostructural Hf and Zr aluminides similar parameters were obtained. In the Hf_4Al_3 and Zr_4Al_3compounds another interesting question of probe segregation into minority phase Hf_3Al_2 and Zr_3Al_2, respectively, occurred when $^{111}In/^{111}Cd$ probes were applied. This topic will be discussed in the Chapter 2.2.

The results of the *ab initio* calculations for the Hf – and Zr – aluminides, performed in corroboration with theory groups mentioned above [Wod07, Err10] and found in the literature [Bel07], reproduce the measured EFGs very well (Figure 2.2). All calculations were done for 0 K, thus the comparison was only possible due to the very precise determination of temperature dependence parameters which allowed to extrapolate the experimental (V_{zz}^{exp}) values to 0 K. (It should be mentioned that the results for some of the compounds have not been published yet). A good agreement between experimental and calculated values is achieved for the ^{181}Ta probe, for which the largest deviation in $|V_{zz}|$ reaches almost 10%. A slightly worse (10-17%), but still acceptable, reproduction of the measured EFGs is obtained for ^{111}Cd probes in the most of aluminides. Only for a few compounds ($HfAl_2$, $ZrAl_2$, Hf_3Al_2, Zr_3Al_2) the largest deviation in $|V_{zz}|$ reaches above 30%.

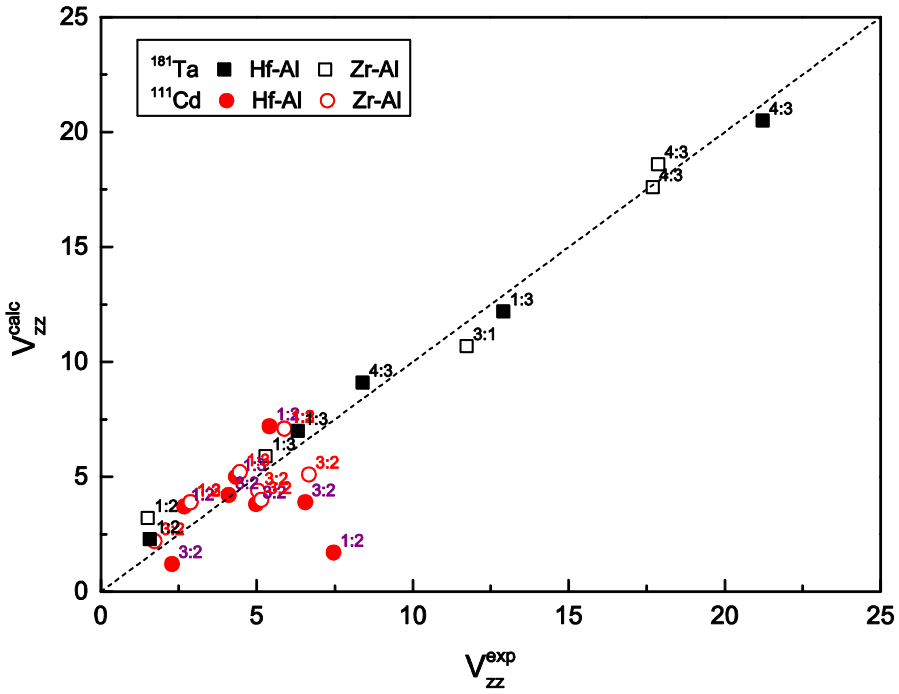

Fig. 2.2. Calculated EFG at Ta (solid symbols) and Cd (open symbols) versus experimental for Hf – and Zr – aluminides. The straight line indicates the ideal 1:1 correlation; the numbers give the atomic ratios of the compound's constituents.

It should be pointed out that the computation at the given site depends on the atom replacing a constituent element, as already mentioned in the case of Zr_4Al_3 compound. Hence, if the probe atoms become impurities in the investigated compound special attention should be paid to this aspect during calculations. The problem of impurity location in the intermetallic systems will be discussed in detail in the following Chapter.

2.2. Lattice location of impurities in intermetallic compounds

A very important problem in the studies of intermetallic compounds is the assignment of a probe location in the crystal lattice. In the PAC method, the number of the observed EFGs and the values of the corresponding *hfi* parameters reflect the position of the probes in the lattice. In particular, the value of the asymmetry parameters, which depend on the local point symmetries, can give information on the probe location. Since the probe atoms are one of the compound constituents or have at least very similar chemical features, the probe positions are unambiguous. Determination of the lattice location of impurity probes can be done in principle through their *hfi* parameter under assumption that the nuclear decay does not change the lattice site of the daughter nuclei. Frequently, the comparison of the atomic volume

and the electronegativity of solute and host atoms can help to attribute the PAC signals to a particular site. On the other hand, the study of Hf and Zr aluminides show that the predictions based only on such arguments are very simplistic and often fail. It has been observed that the site preference can change with composition (especially near compound stoichiometry) [Col01] or temperature [Wod01].

According to the crystallographic data for each structure a certain number of nonequivalent atom positions in the unit cell is available. Each position with certain symmetry could be substituted by the probe atoms and the observed fraction indicates the population of the nonequivalent sites in the matrix. Sometimes the question of probe localization cannot be solved based only on the PAC results, i.e. more than one site have the same symmetry. Thus, in many cases the site of the diluted impurity atoms is hard to predict.

Probe site occupation in the lattice

The Durken-Gurry diagram [Dar57] shown in Figure 2.3 presents a common rule of the possibility to substitute the host atoms in a metal matrix by impurity atoms in a defect-free manner, whenever the electro-negativities and atomic sizes match each other. According to this diagram the comparison of the atomic volume and Pauling electronegativity can give the first suggestion of the possible probe site occupation in the intermetallic systems. Location of the impurity and one of the constituents in the same group of the periodic table, a small difference in the electronegativity and available space at lattice site could clearly favor substitution of certain atoms by the probe atoms.

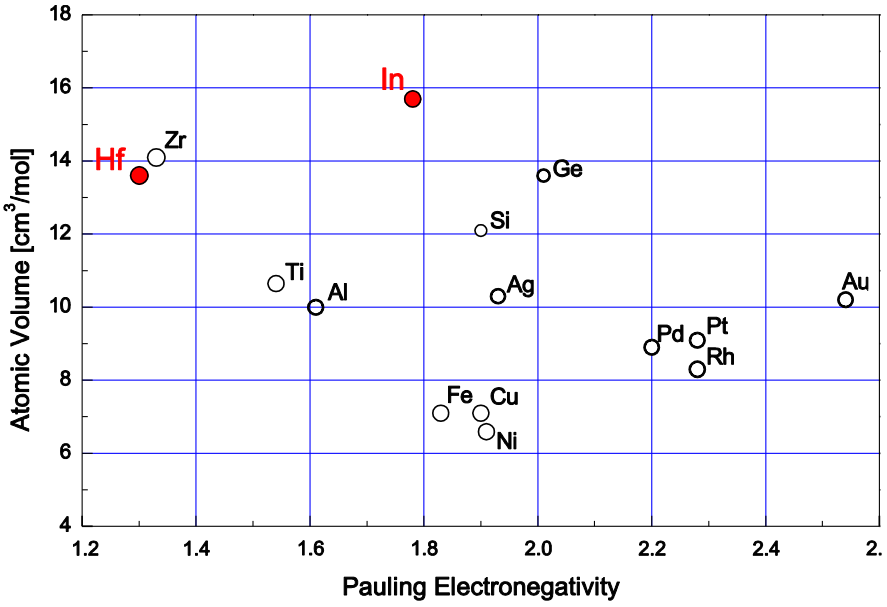

Fig. 2.3. Comparison of atomic volumes and Pauling electronegativities of probe and constituent atoms for different intermetallic compounds.

Hence, the ^{181}Hf/^{181}Ta probes substitute always the Hf, Zr and usually the Ti atoms in different compounds containing one of these elements. It is more difficult to predict the substitution by probe being an impurity in the compound. In the discussed systems, the ^{111}In/^{111}Cd probe was such an impurity and additionally it is larger than all other elements as can be seen in Figure 2.3. In such cases, the probe was found to substitute one or both constituent atoms.

A comprehensive study of the Hf- and Zr- aluminides provided the evidence that ^{111}In/^{111}Cd probe replaced preferably Al atoms. Such behavior was observed e.g. in the Hf_2Al_3, Zr_2Al_3, Zr_2Al, $ZrAl_2$, $HfAl_3$, $ZrAl_3$ and $TiAl_3$ (see Table 2.2. and references therein). Furthermore, in the $HfAl_3$, $ZrAl_3$, $TiAl_3$ compounds, a strong preference for one of the possible Al sites was observed. An identification of the substituted lattice sites was possible thanks to the *ab initio* calculation of the electric field gradient and substitution energy of ^{111}In/^{111}Cd and ^{181}Hf/^{181}Ta at a particular site. Therefore a clear answer of the probe location in the intermetallic compounds cannot be given based only on the measured *hfi* parameters. Additional information such as crystallographic data or the detailed all-electron calculations is necessary.

Site preferences of the impurity atoms

An example of the preferential site occupation by impurity was observed in some Hf- and Zr- aluminides. A combined experimental and theoretical study of the quadrupole hyperfine interactions of ^{181}Ta and ^{111}Cd probes in $TiAl_3$, $ZrAl_3$ and $HfAl_3$ intermetallics allowed to identify the observed hyperfine interactions and to assign them to the particular lattice sites [Wod09, Kul12]. The PAC spectra taken for ^{181}Ta probe in these compounds evidenced a single EFG with a relative width δ of ca. 1%. This reflected a well-defined crystallographic site in the single phase sample. Since Hf and Zr both are isoelectronic and chemically very similar, the ^{181}Hf/ ^{181}Ta probe atoms occupied the substitutional lattice sites. The ^{111}In/^{111}Cd probes are impurities in all investigated compounds. All three non-equivalent crystallographic positions (Hf – 2*a 4/mmm* and Al – 2*b 4/mmm* and 4*d -4m2*) in tetragonal $D0_{22}$ structure are axially symmetric. In the $D0_{23}$ structure two of three Al sites (4*d -4m2* and 4*e 4mm*) as well as the Hf/Zr – 4*d -4m2* site are axially symmetric, while only one Al – 4*c* site has a lower symmetry (*mmm*.). Since in the PAC experiments only one well–defined EFG with δ ~1% was observed [Wod01] the probe site was tentatively assigned to Hf/Zr – 4*d*. But the definitive location could not be determined based only on these considerations.

The subsequent *ab initio* calculation performed for the Hf-Al and Zr-Al systems by H.M. Petrilli and coworkers shed light on the question of the probe

localization in the investigated compounds. In order to estimate the preferred site occupation, the substitution energies were calculated using the expression [Err10]:

$$E_{subst} = E^{tot}_{subst} - E_{imp} + E_X - E_{pure} \quad (2.1)$$

E^{tot}_{subst} is the total energy of the supercell containing a single substitutional Cd atom, E_{imp} denote the energy of the Cd impurity and E_X the energy of the Hf, Zr or Al atom. E_{pure} is the energy of the considered supercell without impurities. E_X and E_{imp} were obtained from metallic Hf, Zr, Al and Cd. A relative difference between the calculated substitution energies indicates that the ^{111}In/^{111}Cd probe prefers to substitute the Al sites in $HfAl_3$ and $ZrAl_3$.

The obtained defect formation energies, i.e. the substitution energies, and the calculated and measured EFG (extrapolated to T = 0 K) in the discussed compounds are collected in Table 2.4. A comparison of the calculated and experimental results achieved for the $TiAl_3$ phase shows the substitution of Ti by ^{181}Ta probe, and preferential occupation of Al – 4*d* site by ^{111}Cd [Wod09].

The interpretation of the experimental *hfi* parameters obtained for ^{111}Cd probes in $HfAl_3$ and $ZrAl_3$ phases, reported in Ref. [Wod01], was refined

Table 2.4. The calculated (V_{zz}^{calc}) values and experimental ($|V_{zz}^{exp}|$) extrapolated to T= 0 K – both in the units of 10^{21}V/m^2 – for ^{181}Ta and ^{111}Cd probe substituting Hf, Zr or Al lattice sites in the XAl_3 compounds (X = Hf, Zr, Ti).

Compound	Lattice site	^{181}Hf→^{181}Ta			^{111}In→^{111}Cd			
		V_{zz}^{cal} [Kul12]	V_{zz}^{calc} [Wod09]	$\|V_{zz}\|^{exp}$	E_{subst} [eV] [Kul12]	V_{zz}^{calc} [Kul12]	V_{zz}^{calc} [Wod09]	$\|V_{zz}\|^{exp}$
$TiAl_3$	Ti 2*a* 4/*mmm*		-15.1	**14.4(2)**	7.2	-4.3	-3.5	
	Al 2b 4/*mmm*		+12.3		2.9	+8.1	+7.5	
	Al 4*d* -4*m2*		-12.9		2.5	**-5.7**	-5.7	**5.0**
$HfAl_3$ ht	Hf 2*a* 4/*mmm*	**-12.2**		**12.5(1)**	5.5	-2.7		
	Al 2b 4/*mmm*	+16.0			4.6	+10.4		
	Al 4*d* -4*m2*	-17.9			4.3	**-6.8**		
$HfAl_3$ lt	Hf 4*e* 4*mm*	***-7.0***		**6.31(1)**	10.2	-1.0		
	Al 4*d* -4*m2*	-14.0			5.5	**-5.0**		**4.34(1)**
	Al 4*c* *mmm.*	+13.3			5.5	**+9.7**		
	Al 4*e* 4*mm*	+14.6			5.7	**+9.7**		
$ZrAl_3$	Hf 4*e* 4*mm*	**-5.9**		**5.28(1)**	10.3	-1.1		
	Al 4*d* -4*m2*	-13.2			5.3	**-5.2**		**4.45(1)**
	Al 4*c* *mmm.*	+11.3			5.3	**+9.7**		
	Al 4*e* 4*mm*	+14.0			5.6	**+9.3**		

according to the new information obtained from the calculations. The main fraction of a well-defined quadrupole frequency ν_Q = 85.0(5) MHz and ν_Q= 86.4(5) MHz in $HfAl_3$ and $ZrAl_3$, respectively, has been attributed now to the Al - site (Table 2.2), instead of the Hf-site, as was suggested in Ref. [Wod01]. Moreover, the comparison of the V_{zz} and E_{subst} values obtained for both compounds indicated the preferential substitution of Al – 4*d* sites by ^{111}In/^{111}Cd probes.

Switching of the probe site in the lattice

In many investigated binary phases, the probes (being an impurity) substituted both constituent atoms sometimes with the preference of one of the available lattice sites. A very surprising temperature behavior of the impurity probe atoms was observed in the ZrAg compound, where changes in solute location between the substitutional sites of the different elements were observed at rising temperature [Kul06].

The PAC spectra taken for the ^{111}Cd probe in the ZrAg sample at the room temperature and 1103 K are shown in Figure 2.4 together with the corresponding Fourier transforms. The room temperature spectrum demonstrated a unique axially symmetric EFG (η=0) with the quadrupole frequency ν_{Q1}= 94.8(5) MHz [Kul06]. The shape of the spectrum indicates a texture of the sample, similarly as was observed in former PAC measurements performed with ^{181}Ta probes [Wod03b]. The measurements at the increasing temperature showed the decrease of a fraction of this EFG and the appearance

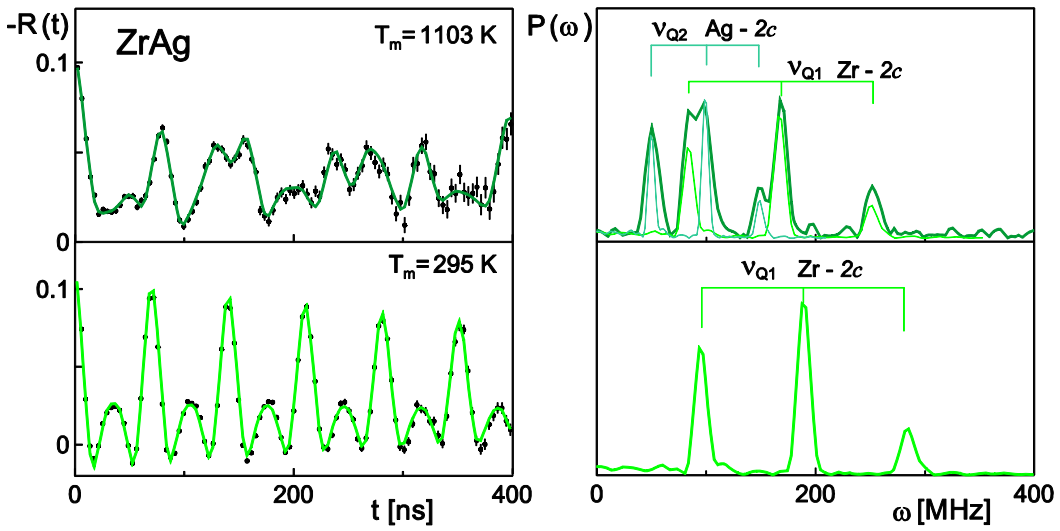

Fig. 2.4. PAC spectra with Fourier transforms taken for ^{111}Cd probe in the ZrAg compound at the indicated temperatures [Kul06].

of the second axially symmetric EFG characterized by ν_{Q2}= 56.5(5) MHz at 873 K. The low values of both distribution widths δ (1-2%) demonstrated the well-defined probe locations [Kul06].

This fully reversible change in the site occupation occurred above 773 K in a rather narrow temperature range as illustrated in Figure 2.5. A ratio of both fractions reached approximately 50% and was then conserved through to the highest measured temperature. Hence, the ^{111}In/^{111}Cd probes can substitute both Ag and Zr. However, it is difficult to correlate the measured quadrupole frequencies with the definite lattice sites relying only on the experimental data, since both the Ag – 2*c* *4mm* and the Zr –2*c* *4mm* sites in the tetragonal B11 structure have the same axial symmetry. According to the Durken-Gurry

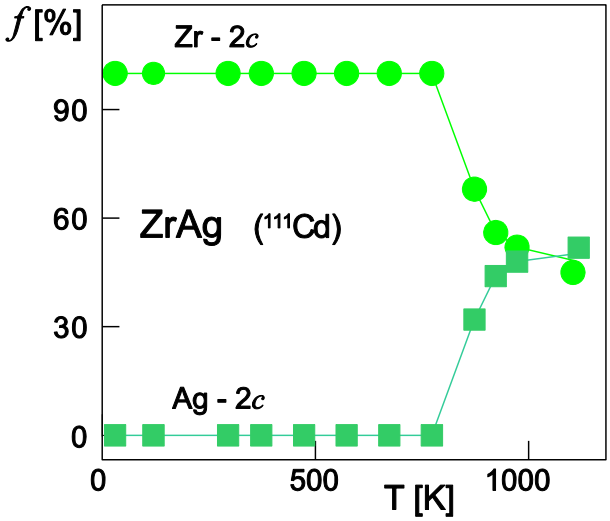

Fig. 2.5. Temperature variation of the probe fractions at the two lattice sites in ZrAg [Kul06].

diagram (Figure 2.3), the difference between the atomic size of indium and the constituent atoms favors the Zr site to be substituted. On the other hand, the thermally expanded lattice enables In to replace Ag – more favorable solution considering the electrochemical factor. Taking into account this argumentation, the attribution of ν_{Q1} to the Zr site and ν_{Q2} to the Ag site is quite reasonable [Kul06].

The confirmation of the site assignment based on the experimental data was possible due to theoretical computation. The *ab-initio* calculations performed by Belošević et al. [Bel08] supported the conclusion that the Ag site is populated only at high temperature, while the Zr site in the whole temperature range. The experimental V_{zz} value obtained for the Zr 2*c* and Ag 2*c* sites and the calculated one match each other very well as presented in Table 2.3.

Table 2.3 Comparison of the calculated EFGs (V_{zz}^{calc}) for ^{181}Ta and ^{111}Cd probes [Bel08] with the experimental values $|V_{zz}^{exp}|$ extrapolated to 0 K [Wod03b, Kul06]; V_{zz} in units of 10^{21} V/m^2.

Compound	Lattice site	^{181}Hf/^{181}Ta		^{111}In/^{111}Cd	
		V_{zz}^{calc}	$\|V_{zz}\|^{exp}$	V_{zz}^{calc}	$\|V_{zz}\|^{exp}$
ZrAg	Zr *2c 4mm*	13.6	13.98(9)	5.1	4.90(2)
	Ag *2c 4mm*			-3.1	2.94(2)

Probe segregation into the minority phase

The other interesting problem of my study, beside the lattice site location, was the preferential location of the probe atoms in the minority phase of the sample being a mixture of two phases. It was not possible to estimate the content of the minority phase in some samples, e.g. ZrAl, Zr_2Ag, by XRD measurements alone. However, the PAC measurements showed the main fraction of the probes located in that small admixture of the minority phase. Two examples of such phase segregation behavior will be presented in the following section.

The ZrAl samples of Al concentration 49.9 at.% and 51.9at.% were prepared by the standard arc melting procedure. The XRD analysis showed formation of the orthorhombic ZrAl compound with the B_f structure and a small admixture of Zr_2Al_3 phase – its content could not exceed a few percent. The Zr-Al phase diagram in the region around 50 at.% Al shows how difficult it was to achieve a single-phase sample. In the case of ZrAl sample even the long-lasting annealing at 1273 K did not improve its purity.

The PAC spectra taken for ^{111}In/^{111}Cd probes in the temperature range 10-1000 K showed that about 50 % of probes exhibited two EFGs characteristic for the Zr_2Al_3 phase (see Table 2.1). The remaining fraction of probe atoms experienced a broad EFG distribution around 100 MHz (a value close to that observed in the isostructural compound HfAl). The measurements were repeated several times with different samples, different heat treatments, and each time very similar spectra were obtained as presented in Figure 2.6. On the other hand, the PAC pattern for ^{181}Hf/^{181}Ta probes in the ZrAl sample exhibits only one well defined nonaxially symmetric EFG (η=0.46(1)) with the quadrupole frequency ν_Q=1065(3) MHz. No evidence of any quadrupole frequency characteristic for ^{181}Ta probe in the tracer phase Zr_2Al_3 was found. Hence, the PAC experiments showed the strong preference of In impurity to locate in the minority Zr_2Al_3 phase in a ZrAl sample [Wod03].

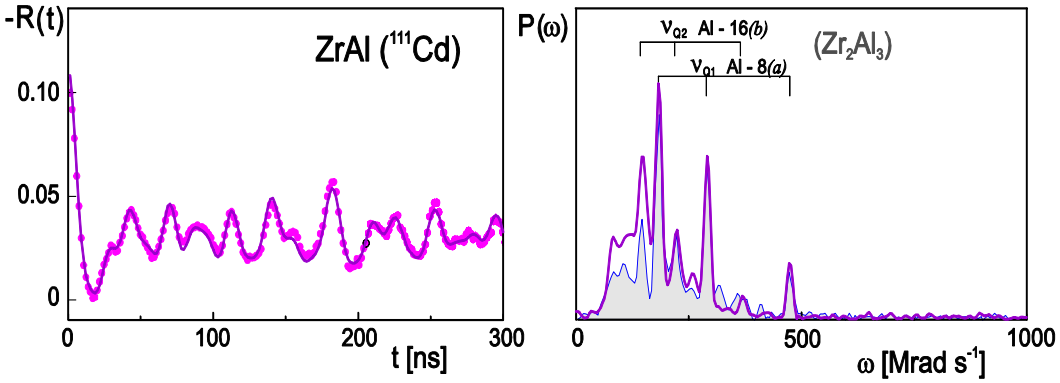

Fig. 2.6. Room temperature PAC spectrum and Fourier transform taken for ^{111}Cd probes in ZrAl sample of 51.9 at% Al. The shaded area denotes the Fourier transform of PAC spectrum taken for Zr_2Al_3 compound [Wod03].

A more complex example of segregation of In solutes in two-phase mixture was observed in the Hf_4Al_3 + Hf_3Al_2 and Zr_4Al_3 + Zr_3Al_2 samples [Err10]. The phase diagrams around 43 at.% Al concentration are rather complicated for both Hf-Al and Zr-Al systems. After different annealing procedures, the XRD spectra obtained for the Hf and Zr aluminides established the existence of two phases: the dominant $(Hf/Zr)_4Al_3$ phase and the minority $(Hf/Zr)_3Al_2$ phase. It should be noted that the PAC measurements done with ^{181}Ta probe in Hf_4Al_3 and Zr_4Al_3 samples did not show any of the quadrupole frequencies characteristic for the Hf_3Al_2 and Zr_3Al_2 phases. Considering the occurrence of the phase mixture and the large number of possible lattice sites in each phase, the analysis of the PAC spectra for the diluted In impurity was very complicated. The fitted results showed evidence for up to five fractions each with different *hfi* parameters. The assignment of the measured EFG to the available crystallographic sites was possible only by performing *ab initio* calculations in all relevant compounds and in the mixed phases. The V_{zz} and η values obtained from the detailed APW+lo calculation for the solute In atoms in the $(Hf/Zr)_4Al_3$ and $(Hf/Zr)_3Al_2$ intermetallics, compared with the PAC results indicated that In prefer to locate in the minority $(Hf/Zr)_3Al_2$ phases (see Table 2.2).

2.3. Temperature dependence of the EFG in the intermetallic compounds

One of the advantages of the PAC method is the possibility to perform a series of in situ measurements over a very wide temperature range and for a long time. The quadrupole frequency value measured in most metals and many intermetallic systems decreases with an increasing temperature. It is

experimentally well established that in most of these systems the dependence follows an empirical $T^{3/2}$ law [Chr76]

$$\nu_Q(T) = \nu_Q(0)(1 - bT^{3/2}) . \quad (2.2)$$

For rare earth and different intermetallic compounds a linear temperature dependence was observed, and the quadrupole frequency values could be fitted with

$$\nu_Q(T) = \nu_Q(0)(1 - aT). \quad (2.3)$$

This indicated that in some cases the mechanism responsible for the EFG temperature behavior may be different.

Both equations could be combined into one simple relation

$$\nu_Q(T) = \nu_Q(0)(1 - BT^{\alpha}) . \quad (2.4)$$

B is a constant in the range 10^{-4} to 10^{-5} K^{α} and in most of cases positive (i.e. EFG value decreases with increasing T). A special attention was paid to experimental results where the ν_Q(T) was established to follow Equation 2.4.

Theoretical investigations [Jen76, Nis78] following the experimental observation of this relation pointed out that temperature dependence of the lattice constant cannot only be responsible for the EFG changes [Rag75, Rag76]. Consequently, it was attempted to combine the phonon models with the lattice and local electron contribution to the main component (V_{zz}) of the electric field tensor to understand this behavior. Using a simple Debye model to describe the phonons, the temperature dependence of the EFG tensor can be well approximated by $T^{3/2}$law as described in Equation 2.2. Nowadays, the EFG as well as phonons can be calculated with a high precision from the first principles (see Chapter 2.1); therefore, some attempts to explain the temperature dependence of the EFG in solids based on the *ab initio* calculation were made [Tor06]. The calculations done for the prototype case of *hcp*-Cd reproduced quite well the experimental trend. Unfortunately, the results were too rough to make statements about the origin of the $T^{3/2}$ dependence and it is still an open question for the theory to explain quantitatively this strong dependence.

Regular – $T^{3/2}$ and linear dependencies

PAC studies over a wide range of the intermetallic compounds show that various types of the temperature behavior are observed. The measurements performed for the Hf-Al and Zr-Al systems provide interesting information

about this problem. For most of the Hf–Al and Zr–Al compounds, the temperature behavior of the EFGs show very similar slope parameters for quadrupole frequencies attributed to the same lattice location of the probes (Figure 2.7). However, the determined *a* and *b* parameters are slightly larger for the most of Zr-Al compounds in comparison with Hf-Al.

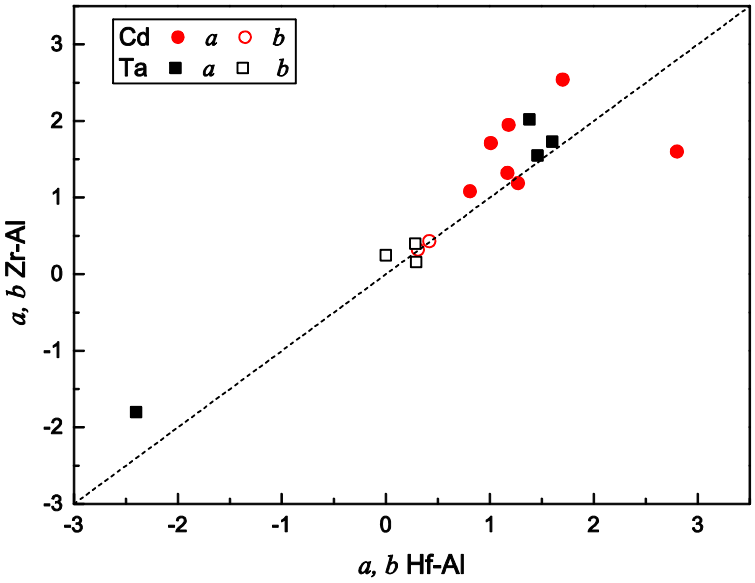

Fig. 2.7. Temperature dependence parameters *a* and *b* for the Hf-Al and Zr-Al compounds deduced from Equations 2.2 and 2.3.

A typical decrease of the quadrupole frequency with temperature according to the $T^{3/2}$ law (Equation 2.2) was observed in the $HfAl_3$ $ZrAl_3$ Hf_4Al_3, Zr_4Al_3 Zr_2Al, Zr_3Al compounds measured at the ^{181}Ta probes and in $HfAl_2$, $ZrAl_2$ measured at ^{111}Cd. However for most of the Hf-Al and Zr-Al phases a linear temperature dependence was observed regardless of the probe used. Equation 2.3 was applied to describe the temperature dependence of the quadrupole frequency observed in Hf_2Al_3, Zr_2Al_3, HfAl, Hf_3Al_2, Zr_3Al_2 for both type of probes. In HfAl and ZrAl only with ^{181}Ta and in $HfAl_3$, $ZrAl_3$, Zr_2Al with the ^{111}Cd probes. The representatives of these two typical decreasing relationships related to Equation 2.4 are presented in Figure 2.8.

For some cases, the EFG changed with temperature very weakly or even remained constant in the wide temperature range such as at site 2*e* in Hf_4Al_3 measured at the ^{181}Ta probe [Wod07] (Figure 2.8a). Sometimes fits of the data using both the linear and $T^{3/2}$ functions were equally correct, and it was impossible to distinguish between these two relations, e.g. in the case of the

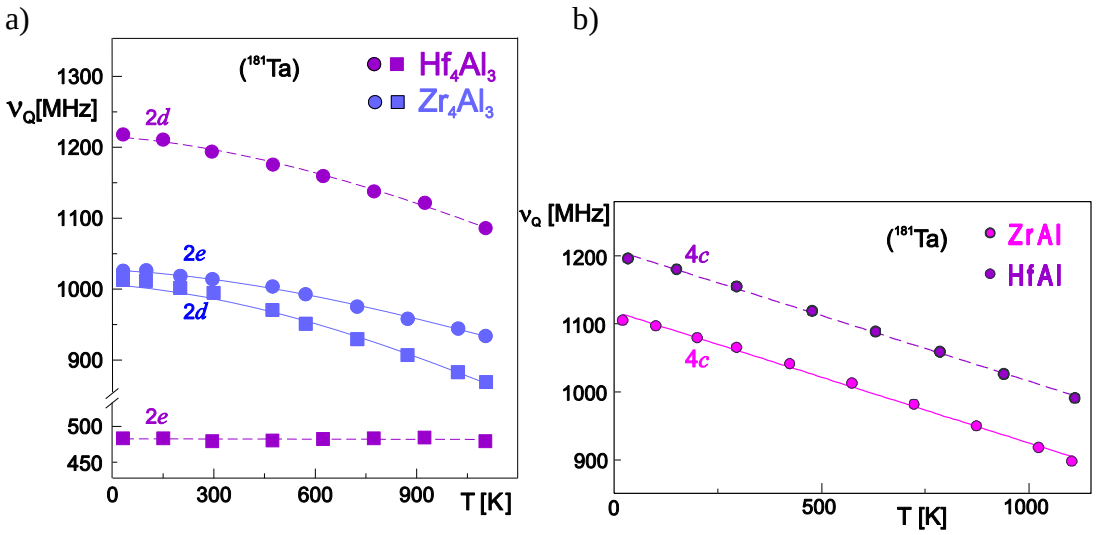

Fig. 2.8. The temperature dependences of quadrupole frequencies following the $T^{3/2}$ a) and linear b) laws [Wod07, Wod03].

temperature variation $\nu_Q(T)$ of the ^{111}Cd probe at Zr – site measured in the ZrAg sample [Kul06].

Well-defined slope parameters *a* and *b* allowed to extrapolate the measured EFG values to T = 0 K and then to compare them to the calculated ones. This helped in the interpretation of the experimental results: the impurity lattice location, site preference etc., as mentioned in previous Chapters.

Anomalous dependencies

The PAC experiments showed that even for compounds with the same crystallographic structure, different temperature behavior of the EFG could be demonstrated, depending on the probe used. Furthermore, the Zr_3Al sample measured with different probes exhibited different temperature dependencies of the EFG at the same 3*c* lattice site as it is presented in Figure 2.9a. Thus, the belonging of alloys to the same type of structure could not help in prediction of the $\nu_Q(T)$ function. The negative value for constant *B* from Equation 2.4, i.e. an increase of the EFG with decreasing temperature, was observed in a few aluminides such as $HfAl_2$, $ZrAl_2$, and Zr_3Al (Figure 2.9a). The rising of the quadrupole frequency noticed in these compounds followed the linear function. However, in some cases, the observed temperature behavior of the EFG was rather unusual, following neither the $T^{3/2}$ nor the linear dependency. Figure 2.9b illustrates the EFG at 2*a* site decreasing with the temperature as the $T^{3/2}$ function (solid symbol), whereas at 2*d* site the EFG changes in a different way. Initially, it decreases down to approximately

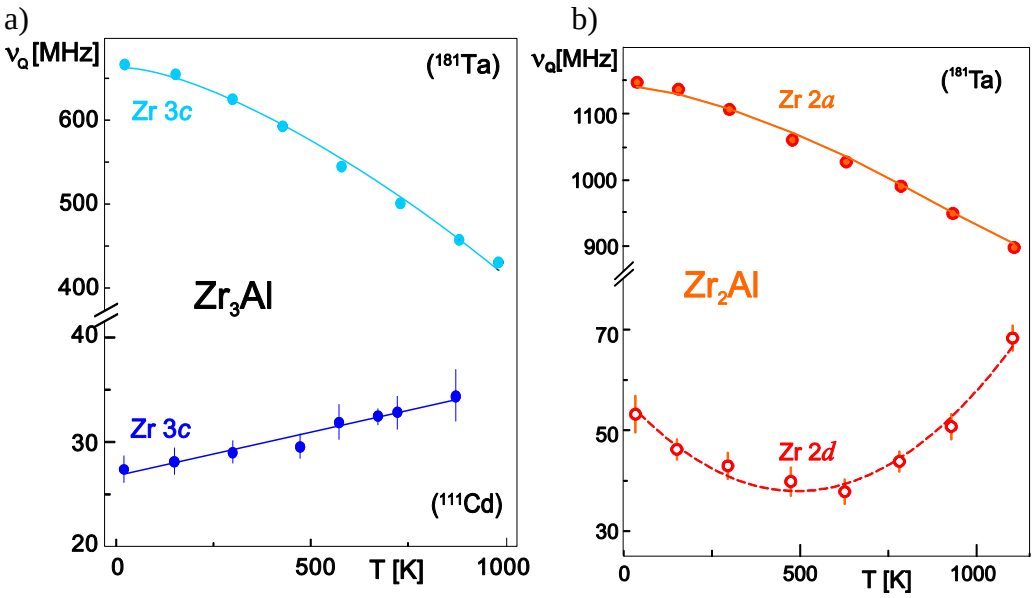

Fig. 2.9. The unusual temperature behaviors of the quadrupole frequency for ^{111}Cd in Zr_3Al and ^{181}Ta in Zr_2Al compounds [Wod04].

500 K, and then shows an increase above this temperature (open symbol) [Wod04]. Additionally, in the compounds where more than one nonequivalent probe site is possible, different dependencies of the EFG corresponding to the different sites have been encountered.

The detailed measurements done for the Hf-Al and Zr-Al systems confirmed that the problem of the EFG temperature dependence in intermetallic system is very complex. This also illustrates the difficulty to find a satisfying theory explaining temperature dependence and allowing the prediction of the EFG value acting on the probe nuclei.

3. Application of PAC in condensed matter and materials physics[2]

Among the numerous experimental techniques available to study solids, the PAC method is widely applied in condensed matter and materials physics. The PAC measurements are unrestricted by temperature or pressure, the concentration of the probe atoms is very low – these properties make PAC favorable tool in the spectroscopic studies. On the other hand, the number of isotopes with nuclear properties suitable for experiments is limited. There are many widely versatile applications of PAC: study of the structural and magnetic phase transitions; phase analysis; surface, interface and grain boundary measurements; study of thin films and nanomaterials; measurements of the diffusion and thermodynamic properties, and many others. Here, I present a few selected cases which illustrate the sensitivity and advantages of this hyperfine method in condensed matter and material physics studies.

3.1. Impurities in solids

The EFG at impurity nuclei in the simple noncubic metals plays a central role in the quantitative understanding of the hyperfine interaction parameters in solids. The interpretation of the PAC measurements requires the understanding of the chemical differences between the probe atom and the constituents of the solids.

[2] This chapter includes data published in [Kul07, Kul10, Kul10a, Kul04, Uhr02, Wod03a], as well as results that have not been published yet. The author contributed substantially to all these works.

Impurity influence on the EFG in TiPd

A PAC study of the TiPd alloy doped with different admixtures showed - besides the martensitic transformation - the influence of impurity on the EFG measured in this compound. The measurements were performed using two most common PAC probes: ^{181}Hf/^{181}Ta probe for the samples doped with Hf and ^{111}In/^{111}Cd for the samples doped with In or Zr. In the experiments for the sample with an admixture concentration $x < 4$ at.%, two nuclear quadrupole interactions were used to described the PAC spectra. Both asymmetry parameters differed from zero, according to the crystallographic structure (B19) of the TiPd low temperature phase. The most populated (main) fraction –denoted EFG1– was attributed to the probes which occupied the Ti – 2*f* lattice site. The measurements performed with the ^{111}Cd probe provided the *hfi* parameters of the main fraction: ν_{Q1} = 48.8(7) MHz and η = 0.34(1) for the pure TiPd compound [Kul10]. The results obtained at ^{181}Ta yielded the ν_{Q1} = 312(2) MHz and η_1 = 0.19(1) for TiPd with the lowest Hf concentration x = 0.18 at.% [Kul07]. The second interaction (EFG2) characterized by a slightly larger distribution of the quadrupole frequencies (ν_{Q2} = 37(2) MHz and ν_{Q2} = 353(2) MHz for ^{111}In/^{111}Cd and ^{181}Hf/^{181}Ta, respectively) was tentatively attributed to the Pd – 2*e* site occupied by the probe atoms.

The *ab initio* calculations of the electric filed gradient at ^{181}Hf/^{181}Ta and ^{111}In/^{111}Cd in the TiPd alloy done by Belosevic at al. [Bel12] confirmed the substitution of Ti site in the lattice by both probes. The comparison of experimental (at the lowest admixture content) and theoretical results are collected in Table 3.1. The replacement of Pd by ^{111}Cd seems to be undoubtful. Different concentration behaviors of the *hfi* parameters describing EFG2 in TiPd doped with Hf compared to other impurity under study could indicate that the ^{181}Hf/^{181}Ta probes do not substitute the well-defined but slightly distorted Pd lattice site.

Table 3.1. The quadrupole frequency ν_Q^{exp}, and the EFG main component (V_{zz}^{exp}) measured at the room temperature [Kul07, Kul10] compared to the calculated V_{zz}^{cal} [Bel12] in TiPd alloys.

Probe	Lattice site	ν_Q^{exp} (RT) [MHz]	$\lvert V_{zz} \rvert^{exp}$ (RT) [10^{21}V/m^2]	V_{zz}^{cal} (0K) [10^{21}V/m^2]	x [at.%]
^{181}Ta	Ti – 2(*f*)	312 (2)	5.47 (3)	5.5	0.18 Hf
	Pd – 2(*e*)	353 (2)	6.2 (5)	-14.1	
^{111}Cd	Ti – 2(*f*)	48.8 (7)	2.43 (3)	2.2	<<0.01 In
	Pd – 2(*e*)	37 (2)	1.84 (5)	1.9	

EFG dependence on the impurity concentration

Figure 3.1. presents the dependence of the quadrupole frequencies (measured at the room temperature) on the impurity concentration in the TiPdX alloys (X = Hf, In, Zr). The value of the electric field gradient acting on the probe at Ti site (EFG1) did not change with the increasing impurity concentration, while the value of the EFG2 increased significantly. Moreover, the V_{zz}(doped)/ V_{zz}(pure) ratio calculated for the admixture concentration ~1 at.% has shown that the EFG2 depends on the type of impurity. The greatest increase was observed up to 1 at.% of the third element. The data obtained for the In and Zr admixtures can be fitted according to the known empirical function $\nu_Q(x) = r(1 - d\ exp(-cx))$ [Bar80]. The determined parameter r reaches 1.43 and 1.3 for In and Zr, respectively, giving the ν_{Q2max} = 58(1) MHz for indium and ν_{Q2max} = 53(2) MHz for the zirconium impurity. The EFG2 measured in the sample with Hf admixture did not follow this relationship. This can indicate that the probes are placed at the interstitial or disordered lattice site.

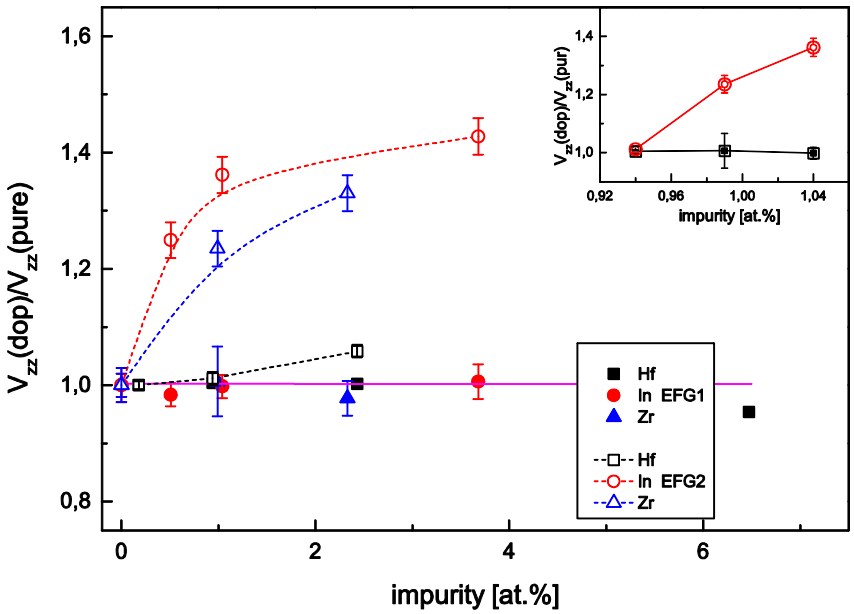

Fig. 3.1. Concentration dependence of the quadrupole frequencies measured at room temperature in TiPdX alloys.

With increasing impurity content, a considerable rise of the distribution width δ around ν_{Q1} was observed for all three elements. This indicates the formation of the lattice site distortions caused by location of the foreign atoms in the crystal cell. The behavior of the parameter δ related to the second quadrupole interaction observed in the TiPd doped with In and Zr differed from the one measured with Hf admixture. The distribution width δ around the

EFG1 decreased with the increasing In and Zr concentrations, but increased with increasing Hf concentration. This observation suggests that the ^{181}Hf/^{181}Ta probes can be located at slightly distorted Pd lattice site.

Impurity influence on the MHF

The PAC method is highly sensitive to the magnetic hyperfine fields (MHF), which in turn reflect the local arrangements of the atoms. Therefore, PAC allows the analysis of the probe's nearest neighborhood. The strength of MHF depends on the chemical character of the probe atom and the number of foreign atoms next to the probes.

Increasing amount of the impurity atoms in the magnetic matrix on the nearest neighbor sites causes the rise of the lower satellite magnetic fields [Neu98, Uhr01, Uhr02]. The fraction of these fields can be estimated by a statistical procedure. If the foreign atoms are isotropically distributed, the probability *P(n)* of finding *n*-atoms in the neighborhood of the probes can be calculated by the binominal distribution function. Thus, the probability *P(n)* can be determined by

$$P(n) = \binom{N}{n} x^n (1-x)^{(N-n)}, \tag{3.1}$$

where x is the concentration of impurity atoms and N is the co-ordination number. The nearest and next nearest neighbors of the probe atoms may be taken into account, if the distance between their co-ordination spheres is very short.

The Fe-Mn alloys obtained by mechanical alloying of the elemental powder were studied with two hyperfine methods: the Mössbauer spectroscopy (MS) and the Perturbed Angular Correlation (PAC). The milled pure Fe sample measured with ^{111}Cd showed the main fraction of the probes in substitutional defect free site in bcc Fe, described by the Larmor frequency ω_L = 560(2) MHz [Uhr01, Uhr02]. This frequency corresponds to the well-known magnetic hyperfine field $B_{0(\mathrm{PAC})}$ = 38.2(2) T [Lin81]. A smaller fraction of the lower magnetic field $B_{\mathrm{def(PAC)}}$ = 35.6(5) T was already observed in other experiments [Neu94] and was attributed to the defects in the nearest neighborhood of the probe atoms. The difference between the strength of the hyperfine field measured with a different hyperfine method is caused by the chemical character of the probe atoms. This problem is known [Kan84] and a factor $fac = B_{0(PAC)}/B_{0(MS)}$ can be introduced to compare the PAC and MS results as done in Table 3.2. It was observed by [Ste66, Vin73], and recently confirmed by *ab initio* calculations [Bła09], that the change of the lattice constant caused by an increasing amount of the impurity atoms in the iron cell

results in the decrease of the hyperfine field compared to the defect free lattice site. Hence, the *fac* is not constant, but changes with an increasing Mn concentration *x* with the rate of-*0.150 T/at.%*.

Table 3.2. The value of the MHFs and the fraction f_n obtained with the PAC and MS methods in Fe-Mn powder [Uhr02]. *N* denotes the number of Mn atoms in the *nn* position.

x	PAC				*P(n)*	MS			*n*	*P(n)*
[% Mn]	B_{PAC} [T]	B_{PAC}/fac [T]		f_{PAC} [%]	N=14	B_{MS} [T]		f_{MS} [%]		N=8
0	38.2(2)	33.0(3)	f_0	85		33.0(3)	f_0	90		
	35.6(5)	30.7(5)	f_{def}	15		29.6(3)	f_{def}	10		
10	37.0(10)	33(1)	f_0+f_{def}	44	23	33.2(3)	f_0	47	0	43
					36	31.0(3)	f_1	32	1	38
	31.3(20)	28(2)	f_1+f_2	46	26	28.5(4)	f_2	19	2	15
	24.9(20)	22(2)	f_3	10	11		f_3		3	4
					3		f_4		4	
15	36.4(10)	33(1)	f_0+f_{def}	24	10	33.1(3)	f_0	23	0	27
					25	31.1(3)	f_1	32	1	38
	30.3(30)	28(3)	f_1+f_2	56	29	28.1(4)	f_2	30	2	24
					21		f_3		3	9
	18.7(20)	17(2)	f_3+f_4	20	10		f_4		4	2

The calculated probability *P(n)* of finding *n* Mn atoms in the probes' neighborhood (Equation 3.1) together with the measured fractions f_{PAC} and f_{MS} are compared in Table 3.2. As expected, the fraction of the defect free site (f_0) decreases with an increasing Mn concentration and simultaneously the probability to find one, two or more Mn atoms (f_1, f_2, f_3, ...) in *nn* neighborhood of the Fe atoms increases. The PAC and MS data agree well concerning the magnitude of the magnetic hyperfine fields B_n, but the particular fractions f_{PAC} and f_{MS} corresponding to these fields exhibit some discrepancies. The observed f_{MS} agree perfectly with the probabilities of the lower magnetic fields estimated from the binominal distribution of Mn atoms (N = 8) (Equation 3.1), while the f_{PAC} match better the *P(n)* calculated for N = 14, i.e. when the next nearest neighbors of the probe atoms were taking into accounts. Each B_{hf}^n was observed with a rather broad distribution width caused by the sample preparation. Hence, the attribution of the f_{PAC} to the sum of two fractions, for which the difference between two corresponding B_n is very small, seems to be reasonable.

The dependence of the MHF on the number of Mn atoms in the probe neighborhood is shown in Figure 3.2. The relative magnetic field B_n/B_0 decreases linearly with an increasing amount of Mn. The constant reduction of the MHF ($\Delta B_n/B_0$ = 0.089(14)) for each Mn atom replacing Fe atom also proves the statistical occupation of the sites. The presented data may also

indicate that the MS method is more sensitive in evaluation of the magnetic hyperfine fields in Fe reduced by the impurity atoms in the first co-ordination sphere, while the PAC is sensitive to a slightly wider region around the probe position.

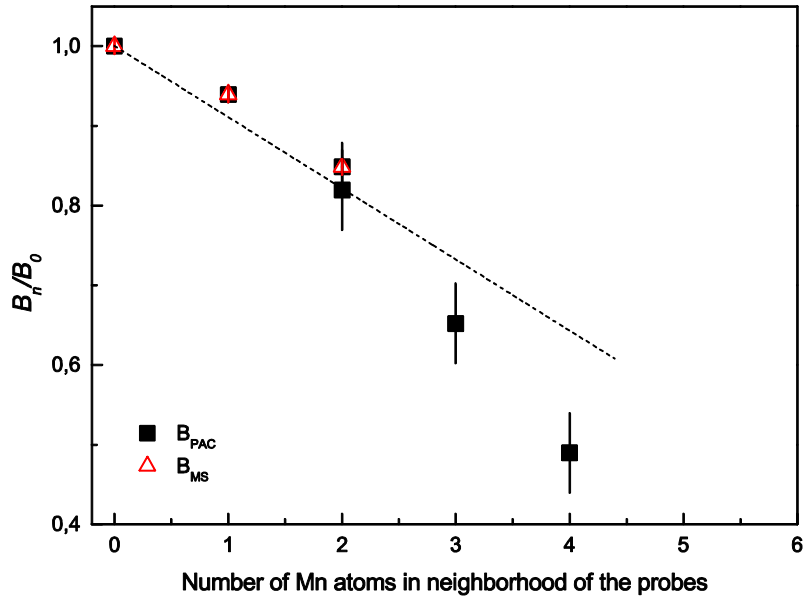

Fig. 3.2. The B_n/B_0 ratio dependence on the number of the Mn "neighbor" atoms.

3.2. Magnitude and texture of the MHF

The magnetism in thin films has been an interesting topic studied for many decades with the use of different experimental techniques. Ion irradiation of the ferromagnetic films can induce or modify their magnetic texture. These ion-induced changes of the magnetic properties can be observed using the PAC method. The application of the microscopic (local) methods in combination with the macroscopic methods, such as the Magneto-Optical Kerr Effect (MOKE) and the Vibrating Sample Magnetometry (VSM), gives complementary information about many aspects of the magnetism in thin films. Various methods were applied by Zhang and coworkers from the Goettingen University for the comprehensive study of changes of the magnetism in the ion irradiated ferromagnetic films.

The PAC method used in my studies of the Ni films gives information on the ion irradiation process itself and radiation defects. As described in Chapter 1.1, the PAC spectra are sensitive to the strength and orientation of the

magnetic hyperfine field ($\boldsymbol{B}_{\mathbf{hf}}$) at the probe position. If the magnetization of all domains is oriented perpendicular to the detector plane, only the term with $2\omega_L$ appears; if it is parallel, only the term with ω_L occurs. The following examples illustrate the influence of ion irradiation on the magnetic texture of the thin Ni films. Furthermore, these cases intend to highlight the most striking experimental results obtained with the PAC method compared with those obtained via MOKE.

Ni films irradiated with heavy ions

The thin (75 nm) Ni films of the size 7x110 mm^2 were deposited via the electron gun evaporation onto the center of a 15x35 mm^2 big Si(100) substrate. The PAC measurements were done with the $^{111}In/^{111}Cd$ probes implanted with the energy of 170 keV into the samples at the room temperature. Then the Ni thin films were homogeneously irradiated with 200 keV Xe^+ ions at 300 K and the dose of $4x10^{14}$ ions/cm^2. The energy of the ^{111}In and Xe^+ ions was chosen to overlap the projected ion range for both ion species and to exclude any ion beam mixing at the film/substrate interface. During irradiation the samples were mounted onto a special holder enabling to keep them either in a *flat* or *bent* position. All PAC measurements were performed at the room temperature before and after each Xe irradiation for the different sample positions and orientations to the detector plane: perpendicular ⊥ or parallel ∥ [Kul04].

After ^{111}In implantation all spectra were fitted with the PAC parameters typical for ^{111}Cd in the substitutional, defect-free sites in Ni (ω_L^{Ni} = 96(2) MHz, corresponding to the magnetic hyperfine field B_{hf} = 6.7(1) T) and with

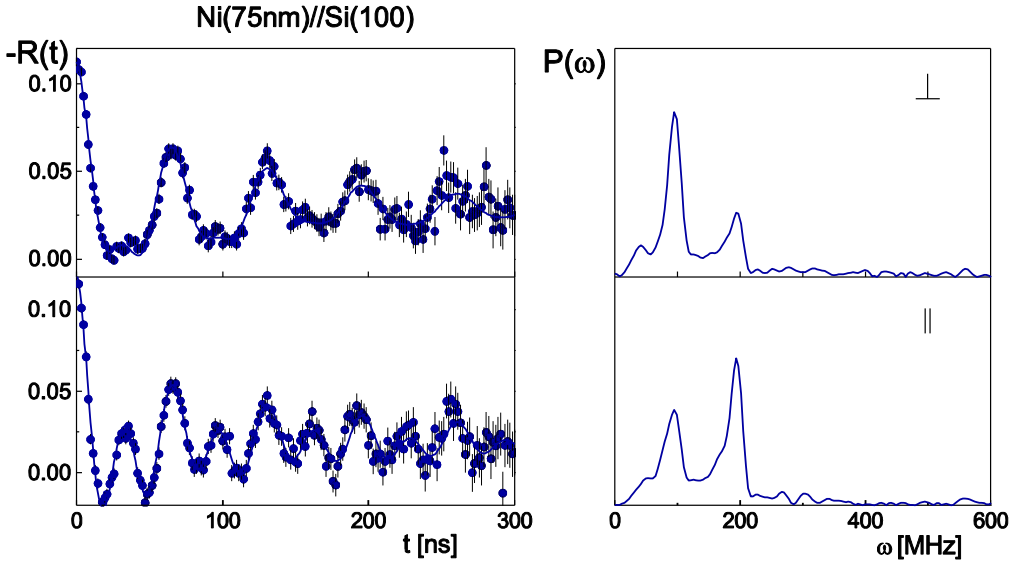

Fig. 3.3. Typical PAC spectra and corresponding Fourier transforms of Ni films measured directly after ^{111}In implantation for two orientations: sample perpendicular (⊥, κ=90°) and parallel (II, κ=0°) to the detector plane.

ω_L = 43(10) MHz [Kul04] characteristic for the probe atoms situated in a trivacancy cluster [Hoh77]. After Xe irradiation another lower MHF occurred and was attributed to the radiation induced defects. The typical PAC spectra with corresponding Fourier transforms taken directly after ^{111}In implantation into the Ni film are shown in Figure 3.3.

To find the direction of the B_{hf} in the Ni thin film without using the external magnetic field, the following experimental set-up was built as sketched in Figure 3.4. The sample was placed perpendicular or parallel to the detector plane and then subsequently rotated by the angle φ relative to the long axis *l*.

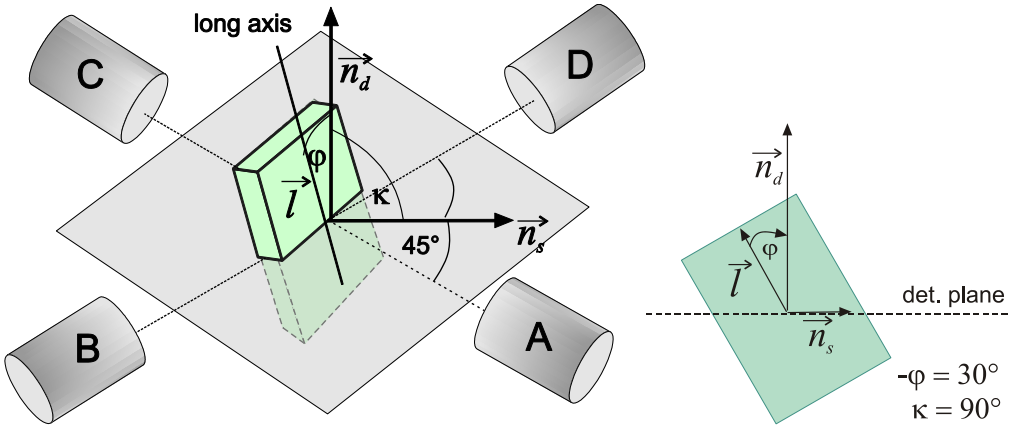

Fig. 3.4. Geometry of the PAC set-up. n_s – normal to the film, n_d – normal to the detector plane, A-D detectors. Here $n_s \perp n_d$, at 45° relative to the detector direction. The sample was rotated around n_s by the angle φ relative to the long axis *l*.

If the magnetic field is aligned within the film plane, its orientation φ_0 (relative to the long axis) can be obtained from the variation of the perturbation function with the tilt angle φ. The intensity ratio of the Fourier components can be expressed as

$$S(\varphi) \equiv I_{2\omega L}(\varphi)/[I_{\omega L}(\varphi) + I_{2\omega L}(\varphi)] = s_{22}/(s_{21} + s_{22}), \qquad (3.2)$$

where amplitudes s_{21} and s_{22} are taken from the fitting procedure of Equation 1.7. The simplest case of a superposition of probe nuclei with an isotropically oriented hyperfine field with a fraction S_0 and nuclei with field oriented at the angle φ_0 with a fraction $(1 - S_0)$ follows the relationship [Kul04]

$$S(\varphi) = S_0 + (1 - S_0)\cos^2(\varphi - \varphi_0). \qquad (3.3)$$

The influence of the external stress on the magnetic texture was observed in a series of the PAC measurements for different sample conditions before Xe irradiation a): *flat* (series I), *bent* (to the well-defined curvatures $1/R = 1.0m^{-1}$) (series II), *relaxed* (series III); after Xe irradiation b): *flat* (series IV); after Xe irradiation of the bent sample c): *bent* (V), *relaxed* (VI). Moreover the PAC spectra were collected with a rotation step 15°-20° to ensure the precise determination of the angle φ_0 [Kul04].

Magnetic texture of the Ni thin film

The measurements with the focused and defocused ^{111}In beam show that already the radioactivity implantation condition can have a direct influence on the magnetic hyperfine field orientation in the thin Ni film. In the standard implantation procedure the focused ^{111}In beam is used, so the PAC spectra exhibit the magnetic texture of the samples shown in Figure 3.3.

Figure 3.5 presents the $S(\varphi)$ function received for the different sample conditions described above. The orientation φ_0 of the magnetic hyperfine field $\boldsymbol{B}_{\mathbf{hf}}$ was obtained by fitting the experimental points to Equation 3.3. The relative orientation of the MHF and the long axis of the sample observed after the indicated sets PAC measurements are shown on the left side of Figure 3.5. No changes of the $\boldsymbol{B}_{\mathbf{hf}}$ direction between the series I (*flat*), II (*bent*) and III (*relaxed*) were observed in the sample before Xe bombardment.

Furthermore, the application of the external stress only does not influence the magnetic hyperfine field orientation within the film plane – $\Delta\varphi_0 = 0°$ (Figure 3.5a). When Xe irradiation was done for the *flat* sample (series IV), the magnetic texture rotated only by $\Delta\varphi_0 = 25(4)°$ (Figure 3.5b). The PAC measurements taken after Xe irradiation of the Ni layer in *bent* condition (series V) followed by the sample relaxation (series VI) show the drastic change of the magnetic texture orientation (Figure 3.5c). This indicates that the compressive stress built up in the Ni film during the relaxation is responsible for the rotation of the B_{hf} direction by $\Delta\varphi_0 = 86(2)°$ [Kul04].

In order to compare the results obtained by the PAC method with the data collected with the macroscopic one, the Magneto-Optical Kerr Effect (MOKE) method was applied to investigate the Ni thin film irradiated with Xe ions. The MOKE measurements were performed for as-implanted and for irradiated samples with in-plane polarization field of $H_{\mathrm{MOKE}} = 1.5$ kOe [Kul04, Mül03]. The polar diagram of the relative remanence $R_e(\varphi) = M_r(\varphi)/M_s(\varphi)$ measured for the relaxed sample is shown in Figure 3.6. The M_r denotes the remanence, M_s – the saturation magnetization, and φ - the angle between the long axis of the sample and the polarizing field H_{MOKE}. The easy axis of the magnetization was found to point into the direction ($\varphi_0 = 22°(2)$), the same as observed by

a) *before Xe irradiation: series I and II*

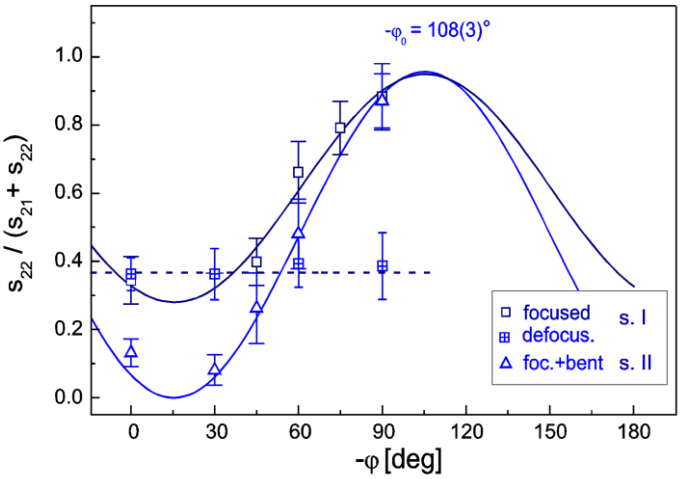

flat, *bent*

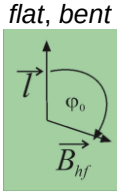

$\Delta\varphi = 0°$

b) *before – series I– and after – series IV– Xe irradiation*

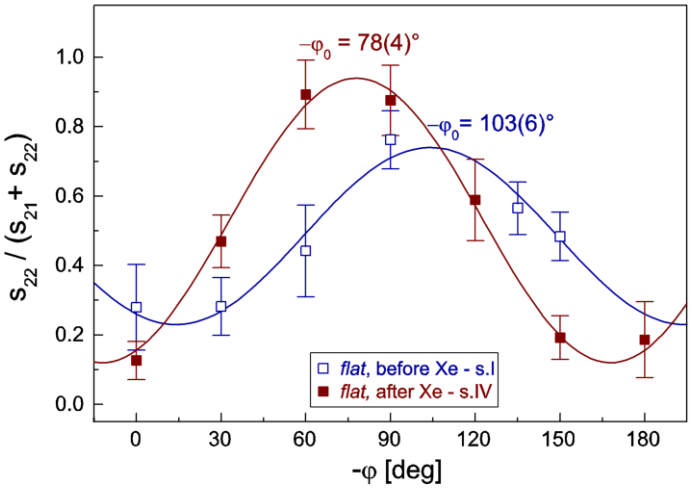

irradiated, *flat*

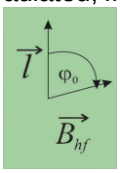

$\Delta\varphi = 25(4)°$

c) *after Xe irradiation: series V and VI*

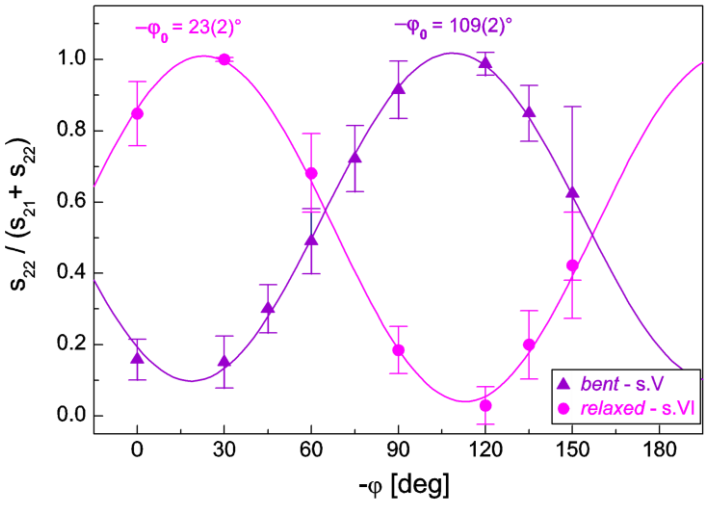

irradiated *relaxed*

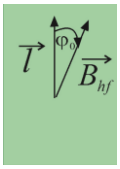

$\Delta\varphi = 86(2)°$

Fig. 3.5. The function $S(\varphi)$ measured for Ni films a) implanted with defocused and focused ^{111}In beam, *flat* and *bent* conditions b) before and after Xe irradiation of the *flat* sample , c) after Xe irradiation in the *bent* condition followed by the sample relaxation.

PAC. Therefore, it was concluded that the hyperfine field in the Ni film was parallel to the magnetization. The PAC method gave the same information as MOKE, but without applying an external magnetic field. This is the main advantage of this hyperfine method.

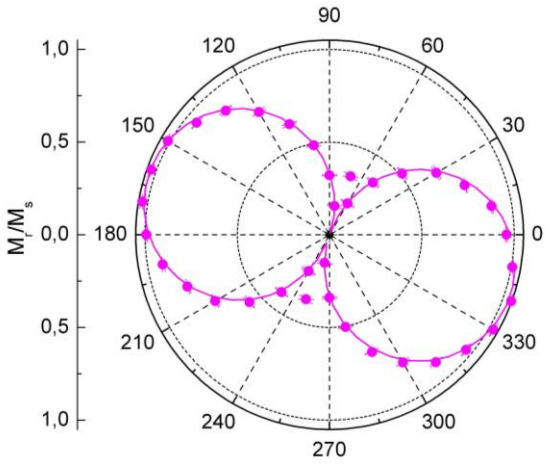

Fig. 3.6. Polar diagram of the relative remanence in a Ni film relaxed after Xe irradiation (series VI).

3. 3. Nanomaterials

In recent years, an interest in the nano-sized particles, nanotubes and the nanocrystalline materials has been exploding. This class of materials offers a very wide field of new applications due to their mechanical, magnetic, optical and other properties, which differ from those of the polycrystals or single crystals. The mechanical alloying (MA) and mechanical milling (MM) processes are the powerful tools for synthesis and fabrication of the advanced materials including equilibrium and non-equilibrium phases, such as amorphous phases or supersaturated solid solutions. They can be used to produce the alloys and compounds that are difficult or impossible to obtain by the conventional melting techniques. Moreover, during milling of the initially crystalline compound a polymorphic or order-disorder phase transitions can occur. After sufficient milling time the phase evolution to amorphous state or decomposition of the intermetallic phase can be achieved. The mechanical alloying process, where a solid state reaction takes place between the fresh powder surfaces of the reactant materials at the room temperature, can be used for the formation of the nanostructured materials.

Nanocrystalline materials are intensively studied using a broad arsenal of techniques, among which the PAC method has a great local sensitivity. Application of the PAC technique should enable the observation of the formation of equilibrium phases, the nanostructure and amorphous phases from the very beginning stage of the milling process.

Mechanical alloying of Fe – Mn

The Fe-Mn alloys are of technological interest, mainly related to the weak shape memory effect arising from the γ-Fe(Mn) fcc – ε-Fe(Mn) hcp martensitic transformation [Ena75], and to the multilayer spin-valve devices. The equilibrium phase diagram of the Fe-Mn system shows existence of three phases: bcc α-Fe, fcc γ-Fe(Mn) and bcc α-Mn at the room temperature. The concentration of these phases (at RT) can be changed by the mechanical alloying procedure, as demonstrated by the X-ray diffraction experiments [Tch99] (Figure 3.7).

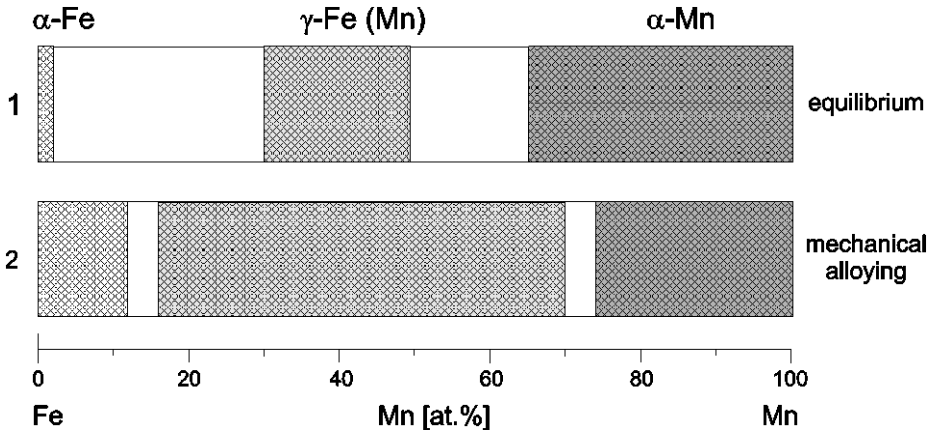

Fig. 3.7. Existence ranges at RT for alloy phases in the Fe–Mn system: (1) alloy formation in equilibrium, (2) alloy formation after high-energy ball milling [Tch99].

In order to study the formation of the Fe-Mn alloys in an extended composition region, the Fe-Mn samples were prepared by 1 hour milling of the high purity iron and manganese elemental powders using a planetary ball mill AGO-2U type equipped with a steel drum and steel balls. The PAC measurement (using ^{111}In/^{111}Cd probe) were performed for the Fe-Mn alloys with the Mn concentration 10-90 at.% and compared with the results obtained by the Mössbauer spectroscopy [Uhr01, Uhr02]. The magnetic hyperfine field for the ^{111}Cd probes on substitutional defect-free sites in bcc Fe is well known (B_{hf} = 38.2 T) [Lin81] and in the PAC spectra it is observed as the large Larmor frequency of 560(1) MHz.

The PAC spectrum taken at the room temperature for the ball milled pure Fe showed mainly the Larmor frequency (ω_L^0=560(1) MHz), which corresponds to the magnetic hyperfine field on the defect-free site in bcc α-Fe. The rest of the probes (about 15%) exhibited a lower MHF (ω_L^{def}=522(6) MHz, B_{hf}^{def}= 35.6(5) T) caused by a defected neighborhood [Uhr02]. These results are similar to those obtained for the thick Fe matrix. With an increasing amount of Mn (up to 15%), the probe atoms with one, two or more Mn atoms as the nearest neighbors were detected, which caused a constant reduction of the MHF. The probabilities for those lower fields could be estimated from the binominal distribution of the Mn atoms, similar to the case of Ni film irradiated with Sb discussed in detail in Chapter 3.1. In the case of pure Mn, the spectra taken for the ball milled and a thick metallic sample were significantly different. Two broad electric field gradient distributions around 72 MHz and 126 MHz, and one quite well defined EFG (ν_Q=102(4) MHz, η=0.65(5)) were required to fit the data of ball milled Mn sample. For the Fe samples with the highest Mn concentrations (80-100 at.%) the same set of parameters was used [Uhr02].

For the samples with the Mn concentration in the range 20-70 at. %, the XRD analysis proved the fcc structure of the γ-Fe(Mn) phase [Tch99]. Nevertheless, the PAC spectra changed between 30 and 40 at.% Mn. The fcc γ-Fe(Mn) phase ordered antiferromagnetically; the possible explanation for this behavior is the change of the Néel-temperature. The PAC measurements indicated that the Néel-temperature for the sample with 30 at.% Mn is below, and for the sample with 40 at.% Mn, above 300 K [Uhr02].

The PAC experiments (and the MS measurements) confirmed that the high-energy ball milling of the Fe-Mn powders results in the alloy formation in the whole concentration range. The phase composition corresponds to the equilibrium phase diagram but with the extended concentration ranges of a single-phase. The Mn atoms were found to be almost randomly distributed in the solid solutions obtained with the milling procedure.

Mechanical alloying of Hf – Al

The powder sample of the $HfAl_2$ compound was synthesized from the powder elements in a planetary mill and then analyzed using the scanning electron microscope, the X-ray diffractometer and the PAC method. The average grain size was determined using the Debye-Sherer formula based on the broadening of the X-ray diffraction peaks [Sur98] that correspond to a certain phase. The grain size of the $HfAl_2$ powder reached the mean value of approximately 65 nm [Kul10a].

The PAC spectrum, taken directly after the sample activation, exhibited only a broad distribution of the EFGs without any signal from the stoichiometric Hf-Al phases. Successive annealing up to 900°C (in vacuum) did not improve the signal. On the other hand, the XRD analysis showed for the "as prepared" sample the reflexes from the $HfAl_2$ phase. Additionally, one could identify peaks from the Hf_2Al_3 and $HfAl_3$ admixture. After the annealing procedure mainly the reflexes characteristic for the $HfAl_2$ compound were observed (Figure 2 in Ref. [Kul10a]). Such different results of the XRD and PAC measurements led to conclusion that the grains of $HfAl_2$ nanopowder are too damaged to exhibit a clear electric field gradient.

Ball milling of Hf-Al compounds

In order to determine the limit dimension of the sample particles for the clear PAC signal, the bulk $HfAl_2$, $HfAl_3$ and Hf_2Al_3 samples were successively grounded in the high energy ball mill SPEX 8000 equipped with the acrylic vial and two 1/4 inch-diameter tungsten carbide balls. The room temperature PAC spectra were taken for "as-prepared" sample and after each milling step. In order to remove the damages caused by milling procedure, the additional annealing was performed after the last milling step. The hafnium aluminides were already the subject of the former PAC investigations. Therefore, the EFG

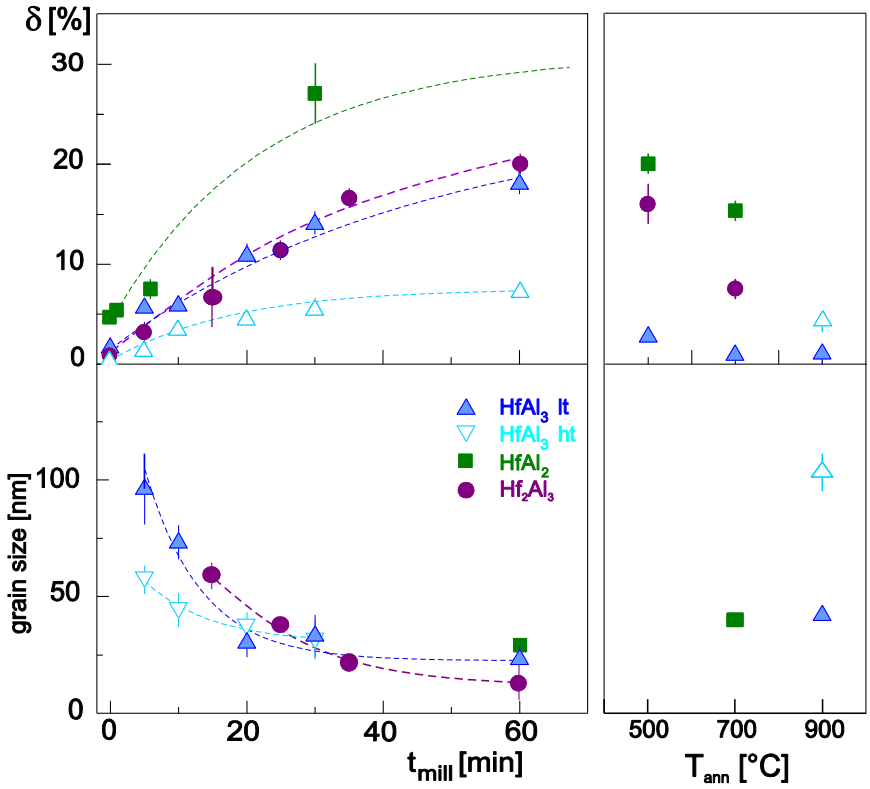

Fig. 3.8. Influence of the milling time t_{mill} and annealing temperature T_{ann} on the frequency distribution widths δ and average grain size in Hf – Al samples.

parameters characteristic for all these compounds are well known (see Table 2.1 in Chapter 2.1). Thus, in the PAC measurements of mechanically alloyed sample each alloy should be easily identified. Moreover, the XRD measurements were performed after each subsequent milling step to determine the average grain size of the observed phase.

Figure 3.8 presents the influence of the milling time on the frequency distribution width δ and the average grain size obtained in the investigated compounds. For all samples together with the increasing milling time, the grain dimension decreased drastically during the first 30 minutes to reach about 30 nm in size. The further 30 minutes of milling did not significantly reduce their dimension. The δ value decreased continuously with the milling time. In order to check that the defects at the grain boundaries are responsible for the largely distributed EFGs, the samples were annealed at elevated temperature for 24 hours after the final milling step. The decrease of the distribution width was observed for all measured samples (to the right in Figure 3.8). This indicated the reduction of the structure damages close to the probe.

Furthermore, the fraction of the probe atoms located in the undamaged crystal structure subsequently decreases with the milling time (Figure 3.9). After 60 minutes of milling more than 50 % probes still exhibit the EFG characteristic for the bulk $HfAl_3$ and Hf_2Al_3. For $HfAl_2$, a very broad distribution of the quadrupole frequency around the value typical for the bulk sample was observed already after 30 minutes of milling. The final heat

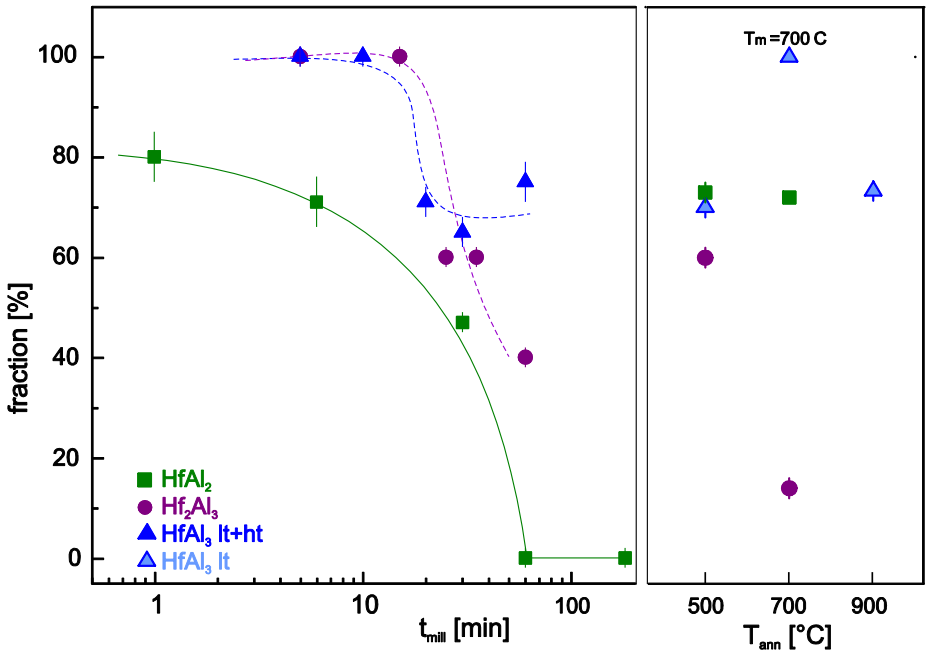

Fig. 3.9. Fraction of probes in undamaged regions in ball milled Hf – aluminides measured at RT as function of the milling time t_{mill} and after annealing.

treatment applied after milling procedure caused a different process observed in each samples: a removal of defects, recrystallization or phase decomposition.

The $HfAl_2$ powder formerly milled for 180 minutes was heated at 700°C. The PAC measurements showed that the thermal treatment partially removed the defects in the crystal structure and the frequency distribution became close to that for the not milled sample. The fact that the annealing procedure did not "repair" the $HfAl_2$ structure in the whole volume fraction indicates a significant structural disorder in the outer part of grains [Kul10a].

For the bulk $HfAl_3$ sample two EFGs were observed – the main fraction of probes exhibited an EFG corresponding to the low temperature $D0_{23}$ phase, the remaining fraction to the high temperature $D0_{22}$ phase. Both phases were observed in the PAC measurements as well as in the XRD spectra for the whole milling program. But only the annealing at 500°C after 60 minutes of milling led to the PAC spectrum with the well-defined quadrupole frequency typical for the low temperature $HfAl_3$ phase. Lack of the high temperature phase proves that the defects in the crystal structure created during milling facilitated the recrystallization of the sample in the $D0_{23}$ phase. Additional annealing at 900◦C followed by a fast cooling down again caused the formation of a small fraction (ca. 20%) of the $D0_{22}$ phase. It should be mentioned, that the heating treatment alone (500°C 47h) without any ball

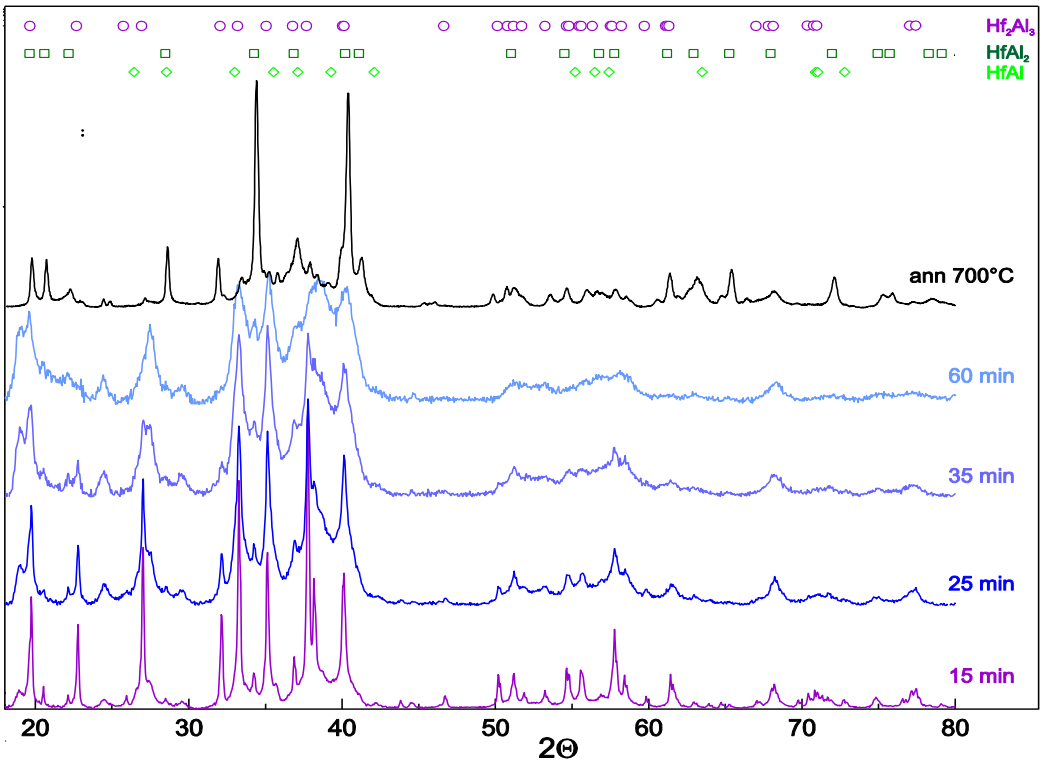

Fig. 3.10. XRD spectra for Hf_2Al_3 sample measured after subsequent milling steps, and final annealing of the powder after 60 minutes milling time. Peaks corresponding to the initial Hf_2Al_3 and the final HfAl and $HfAl_2$ phases are indicated.

milling procedure did not remove the high temperature fraction from the bulk sample [Kul10a]. The XRD measurements confirmed the presence of both phases in the milled $HfAl_3$ sample.

The ball milling of the Hf_2Al_3 bulk sample caused the fraction reduction of the well-defined quadrupole frequency already after 25 minutes of the total milling time. This fraction increased again in the sample milled for 60 minutes and annealed at 500°C. Surprisingly, after additional heating at 700°C the PAC spectrum changed drastically. The main fraction (~60%) was described by the *hfi* parameters well known for the $HfAl_2$ compound. About 26% of probes exhibited the EFG similar to that observed in the HfAl compound, and only 14% of probes still were placed in the Hf_2Al_3 phase. These measurements showed that the milling process followed by an additional thermal treatment caused the decomposition of the initial Hf_2Al_3 phase into $HfAl_2$ and HfAl. The possible explanation of the observed phenomena is the increase of the local temperature above the melting point and high stress built during milling. In the XRD spectra the change of the sample structure was identified and the lines characteristic for the $HfAl_2$ phase were seen, in agreement with the PAC results (Figure 3.10).

3.4. Oxidation of the intermetallic compounds

Oxidation is generally described as the most commonly encountered form of the high-temperature corrosion. However, the oxidation process itself is not always detrimental. Corrosion studies of the intermetallic compounds are motivated by two needs for (i) high melting, hard materials which form protective films to operate at high temperatures in the corrosive environments; (ii) the surface examination of the semiconductor compounds to fabricate the electronic materials. The oxidation process is usually selective; preferentially forming the oxide of the less noble constituent and for the refractory intermetallic compounds shows a tendency to form more than one type of the oxide at low temperatures.

The PAC technique is very suitable in the investigation of the oxidation processes since it enables observation at a very early stage. The measured EFG is mainly determined by the positions and charges of the neighbor atoms. New microsurroundings arising around the probe site cause changes in the EFG value and symmetry and can be identified by their characteristic hyperfine interactions parameters.

EFG at ^{181}Ta probe in Hf-, Zr- and Al- oxides

Intermetallic compounds are being considered as an important class of materials for a variety of applications. The alloys based on the aluminides have gained a special attention due to their high oxidation resistance. The ZrAl, Zr_4Al_3, Zr_3Al_2 and Zr_3Al samples were subsequently annealed for 3 hours in air at the increasing temperatures from 973 K to 1373 K. At the end, they were additionally heated in air for 24 hours at 1373 K. After each annealing step, the PAC spectra were recorded at the room temperature using a conventional fast-slow coincidence setup with four BaF_2 detectors. The known quadrupole interaction parameters of the ^{181}Ta probes in the ZrAl, Zr_4Al_3, Zr_3Al_2 and Zr_3Al compounds listed in Table 2.1, Chapter 2, and their constituents oxides (Table 3.3) were used for the identification of the probe surroundings created in the investigated samples.

Figure 3.11 illustrates the evolution of the Fourier transform of the PAC spectra taken at the room temperature with the ^{181}Ta probes in the $ZrAl_3$ sample after annealing in air at the increasing temperature. For the oxidation at T_{oxid} = 973 K one can observe a single frequency triplet indicating a unique EFG whose parameters are known for the non-oxidized Zr_3Al. This indicates that the ^{181}Hf/^{181}Ta probes occupy the defect-free substitutional Zr lattice sites in the Zr_3Al lattices. For higher heating temperatures, the fraction of the probes in pure Zr_3Al decreases and two new fractions appear. One fraction of

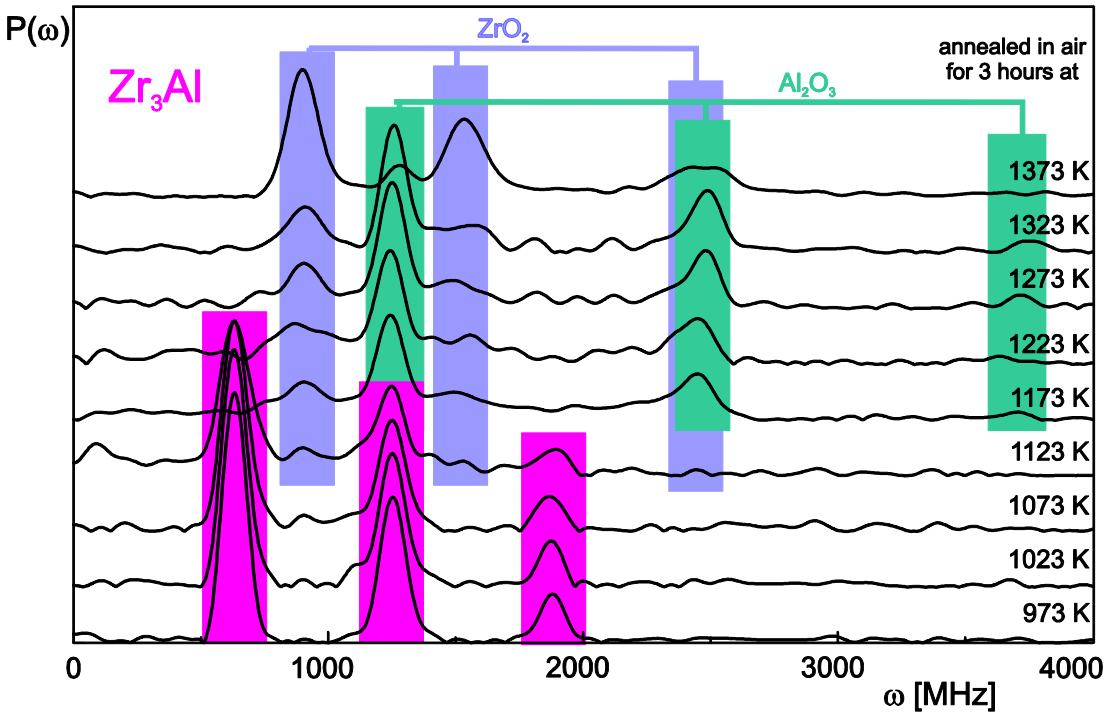

Fig. 3.11. The Fourier transforms of PAC spectra for ^{181}Ta probe in Zr_3Al sample oxidized in air at the indicated temperatures. The quadrupole frequencies ν_Q characteristic for Zr_3Al, ZrO_2 and Al_2O_3 are indicated by the color bars [Wod03a].

the probes experiences the EFG characterized by ν_{Q1} = 777(3) MHz, η_1 = 0.39 and the second one by $\nu_{Q2} \approx$ 1250(3) MHz, η_2 = 0 [Wod03a].

In order to assign these EFGs to the specific probe surroundings, the known results of the measurements at ^{181}Ta in the HfO_2, ZrO_2 and Al_2O_3 phases were considered, see Table 3.3. This table collects also theoretical results for the EFG tensor (V_{zz} and η) at the Ta site in the investigated oxides obtained by the all-electron *ab initio* electronic structure calculation, published elsewhere. The literature on the subject reports that the charge state of impurity can modify the electronic structure around the impurity. Consequently, this change can strongly affect the structural distortion and the EFG [Alo08, Dar12, Err02, Err03]. Considering that the replacement of Hf^{+4}, Zr^{+4} or Al^{+3} by Ta^{+5} can lead to the different charge states, calculations were performed assuming that neutral Ta remains in the valence state when replacing a host atom ("*neutral state"*) and removing one or two electrons from the unit cell (*"charged state"*). For the computation details see Refs. [Ren05, Alo08, Tay10, Tay12].

Table 3.3. Experimental and calculated V_{ZZ} value, in units of 10^{21} V/m^2, and the asymmetry parameter η at the ^{181}Ta site in in the *m*-HfO_2, *m*-ZrO_2 and α-Al_2O_3 oxides.

Oxide	Exp.			Calc.		Ref. exp.	Ref. calc.
	ν_Q[MHz]	V_{zz}^{exp} (RT)	η (RT)	V_{zz}^{calc} (0K)	η^{calc}		
m-ZrO_2	783(6) 802(2) 1200(100) 777(3)	13.7(1) 14.1(1) 21(2) 13.6(1)	0.337(7) 0.335(5) 0.3-0.4 0.39(3)	13.49 *char* 19.93 *neut*	0.3(1) 0.4(5)	[Sci85,Jae86] [For08] [For08] [Wod03a]	[Tay12] [Tay12]
α-Al_2O_3	1250(3) 628(5)	21.9(1) 11.0(2)	0 0	19.85 *char* 10.61 *neut*	0 0	[Wod03a] [Ren05]	[Ren05] [Ren05]
m-HfO_2	793(2) 1300(100)	12.4(1) 13.9(1) 23(1)	0.340(3) 0.345(5) 0.3-0.4	13.6 *char* 21.2 *neut*	0.40 0.29	[Aya94] [For08] [For08]	[Alo08] [Alo08]

The measurements at ^{181}Ta in HfO_2 gave a large fraction of the probes having an asymmetric EFG with the quadrupole frequency ν_Q = 707-802 MHz [Aya94, For08] which has been attributed to a substitutional defect-free cationic site in the monoclinic oxide structure. The PAC experiments on ^{181}Ta in ZrO_2 showed a very similar EFG, ν_Q = 783(6) MHz, η = 0.34(1) [Sci85, Jae86], which was also attributed to the substitutional 4*e* cation site (Table 3.2) basing on the chemical and structural similarities between both compounds. Considering the experimental and calculated results, the first

EFG1 (V_{zz} = 13.6x10^{21}V/m^2) was connected with the formation of monoclinic ZrO_2 and attributed to Ta in a regular cationic site with the probe in the charged state.

In the Al_2O_3 corundum structure, each cation is surrounded by a nearly regular oxygen octahedron with a rather small bond length between the cationic and the oxygen ion. The combined experimental and *ab initio* approaches were used to characterize the EFG for the ^{181}Ta probe in the α-Al_2O_3 single crystal [Rent05]. The calculated value of the symmetry and orientation of the largest EFG component V_{zz} for the neutral cell agree excellent with the experimental results obtained for the α-Al_2O_3 single crystal [Ren05], see Table 3.2. The calculated values of V_{zz} and η for the charged cell (V_{zz}^{cal} = +19.85×10^{21}V/m^2, η^{cal} = 0) indicate that the ionization of the deep double-donor level duplicates the magnitude of the EFG but does not change its symmetry.

The second EFG2 observed in the oxidized compound corresponds neither to the experimental results obtained for ^{181}Hf/^{181}Ta in the α-Al_2O_3 single crystal nor to the calculated V_{zz} value considered for the neutral cell. On the other hand, it meets very well the case of the V_{zz} value calculated for a charged cell [Rent05]. Taking into account all these experimental and calculated results, the attribution of the measured V_{zz} = 21.9(3) x10^{21} V/m^2 to ^{181}Ta replacing an Al atom in the Al_2O_3 charged cell is the most probable configuration.

Oxidation of the zirconium aluminides

The influence of the oxidation process on the zirconium aluminides was observed during heating in air at temperatures above 1000 K. The *hfi* parameters assigned to Ta in the regular cationic sites of the monoclinic *m*-ZrO_2 and the corundum α-Al_2O_3 phases with the probe in the charged state discussed earlier were obtained in all oxidized compounds under study. Figure 3.12 shows the probe fractions *f* (left) and the widths δ of the EFG distributions (right) in the ZrAl, Zr_4Al_3, Zr_3Al_2 and Zr_3Al samples after annealing in air for 3 hours at the indicated temperatures. The additional points at 1373 K in the Figure 3.12 correspond to the final oxidation time of 24 hours.

The results show that the limiting temperature for the oxidation resistance of the investigated Zr–aluminides is about 1073 K. The complete oxidation temperature depends not only on the aluminum content in the alloys but also on the c/a ratio of the crystal lattice (Figure 3.13). The obtained values of the probe fractions, however, have to be considered with caution, since the ^{181}Hf/^{181}Ta probes are impurities in both oxides. This fact implies a possible

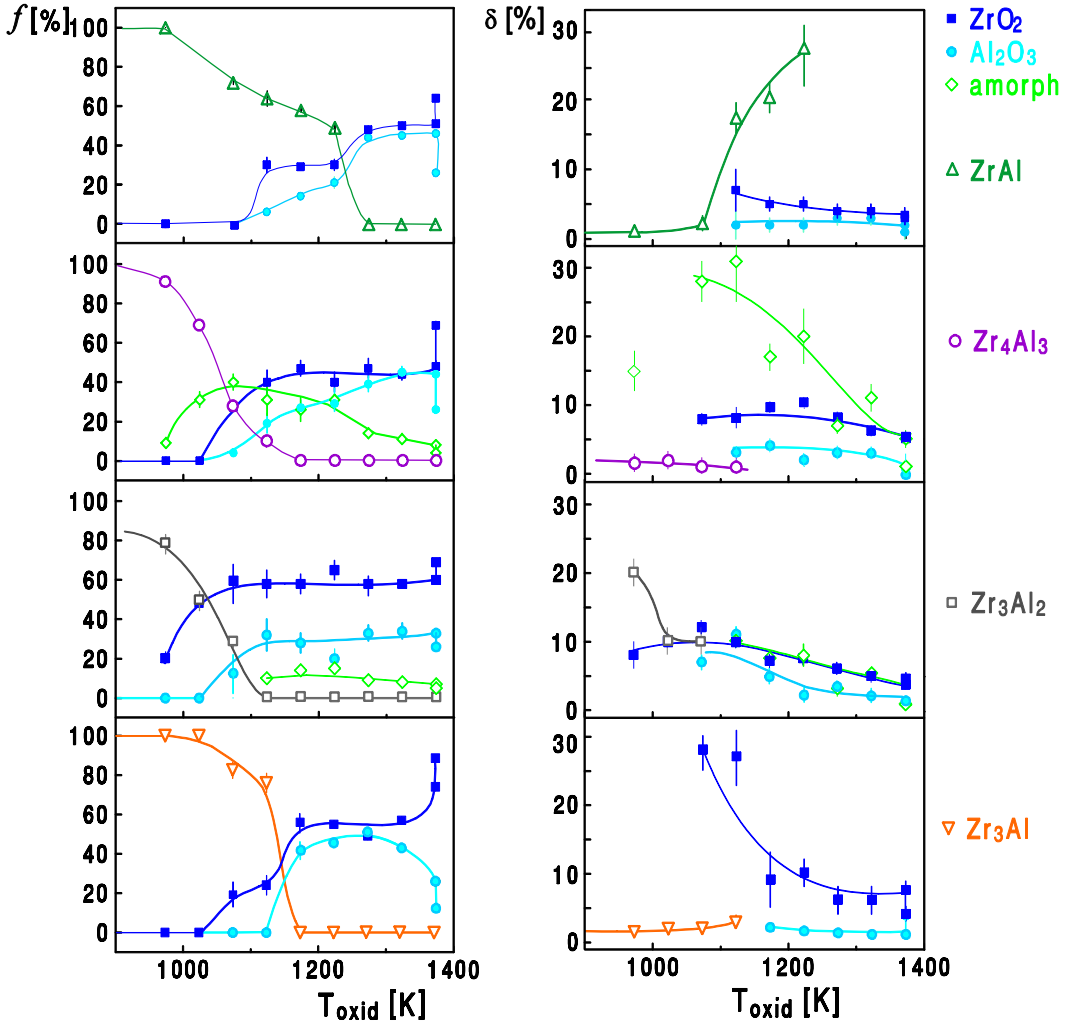

Fig. 3.12 The probe fractions f (left) and widths δ (right) of EFG distributions for ^{181}Ta probes in ZrAl, Zr_4Al_3, Zr_3Al_2 and Zr_3Al samples taken after heating them for 3 hours in air at T_{oxid} temperatures. Additional data for T_{oxid} = 1373 K correspond to the oxidation time of 24 hours (partially adopted from [Wod03a]).

site preference of the probes and in consequence can lead to the quantitatively disturbed fraction behavior. A simultaneously observed decrease of the distributions of frequencies attributed to both oxides indicates the progressive formation of the stoichiometric ZrO_2 and Al_2O_3 and the growth of their agglomerations in the samples. The ratio of both oxides – f_{ZrO2} and f_{Al2O3} formed in the samples reached almost 3:1 after the final oxidation.

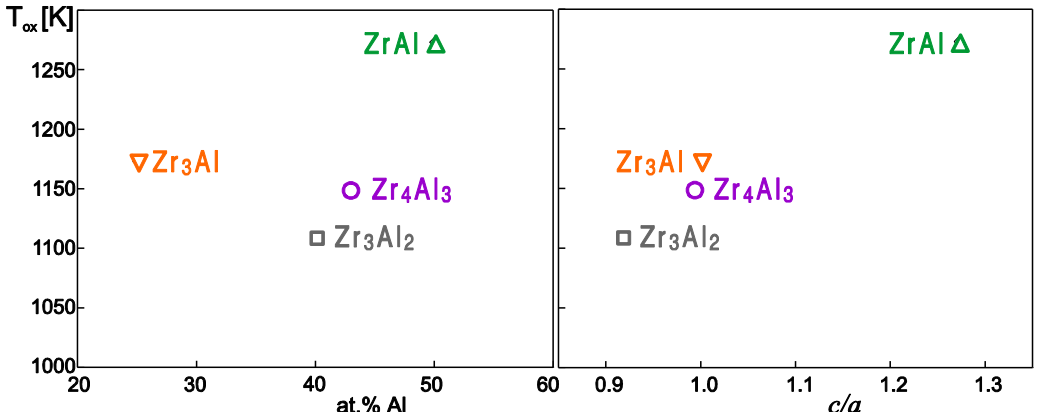

Fig. 3.13 The *c/a* and concentration dependency of the complete oxidation temperature T_{ox} in Zr-Al compounds.

3. 5. Phase transformation

The crystal structure and the properties of the intermetallic compounds at equilibrium are well defined. If the arrangement of the atoms changes with e.g. the temperature, pressure, stress or magnetic field, then the crystal structure of the compound changes, and a transformation takes place. In the intermetallic compounds many transformations like the phase transition, polymorphic changes, order-disorder or martensitic (diffusionless) transformation may occur. The PAC method can be used to follow the changes in the crystallographic structure after the heat treatment, thus to determine the temperature of the phase transformation.

The martensitic phase transformation is a transformation from a low temperature martensitic phase to a high temperature austenite phase. The reversible transformation from austenite to martensite exhibits a characteristic hysteresis loop. In connection to the martensitic transformation a complex bulk of phenomena is observed, known as the shape memory effect (SME) i.e. the effect of restoring the original shape of a plastically deformed sample. Unique classes of the metal alloys, which demonstrate the SME, belong to a group of the smart materials, so-called the shape memory alloys (SMA). To characterize the SMA it is necessary to find i) the temperature for which the formation of martensite and austenite starts and finishes (M_S, M_F, A_S and A_F, respectively) and ii) the width of the hysteresis loop (T_H). The SME can be induced not only by the thermal treatment, but also by the applied magnetic fields and the mechanical properties of materials.

Shape memory alloys are very important for the technological applications, including the mechanical actuator devices, electronics, and medical stents. It is

well-known that by adding an alloying element or by applying a thermomechanical treatment (that introduces precipitates or defects) one changes the transformation temperature [Eck76, Hos96, and Kaw06].

Martensitic transformation in TiPd

The hyperfine PAC method was applied to investigate the phase transformation in the Ti- based intermetallic compounds. The TiPd shape memory alloys are well-known as the potential materials for the high temperature application, since they undergo the martensitic transformation around 800 K [Don70]. The series of PAC measurements with small temperature steps (5–10 K) enabled a very precise determination of the phase transition parameters: the martensitic start temperature (M_S) and the width of the hysteresis loop (T_H) [Kul07, Kul10]. Both PAC probes, ^{181}Hf/^{181}Ta and ^{111}In/^{111}Cd, were used to study the impurity concentration influence on the martensitic transformation parameters. The *hfi* parameters obtained for both probes in the TiPd alloys, and their impurity concentration dependencies were discussed in details in Chapter 3.1.

The change of the probes environment in result of the phase transition appears as the change of the PAC spectra shape. Figure 3.14 shows the temperature behavior of the PAC spectra with a corresponding Fourier

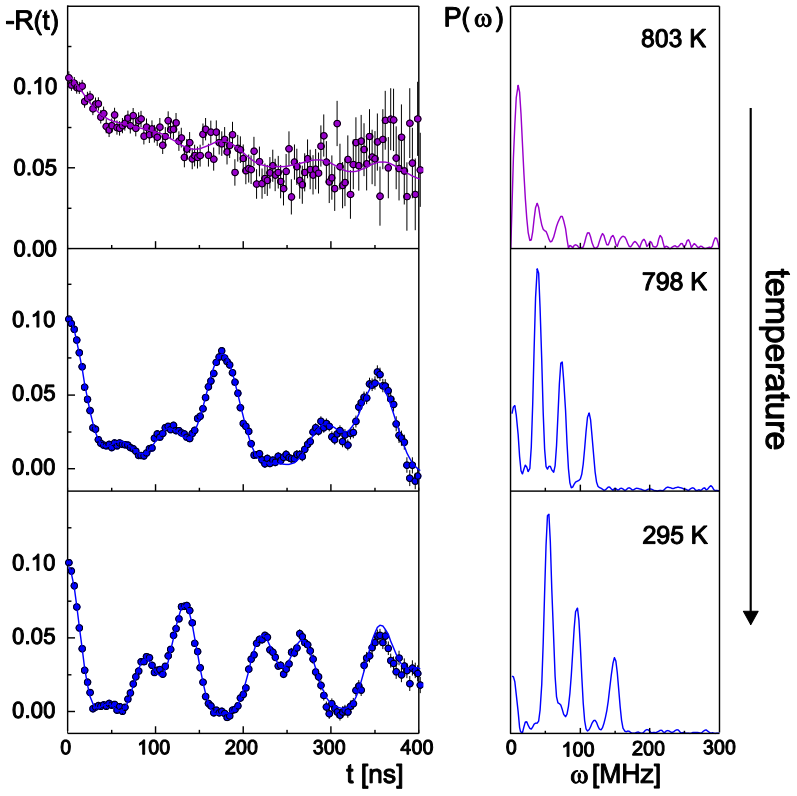

Fig. 3.14. PAC spectra with corresponding Fourier transforms taken for ^{111}Cd probes in pure TiPd sample upon cooling [Kul10].

transforms obtained with the ^{111}Cd probe in the pure TiPd sample [Kul10]. The phase transformation is very well illustrated by the drastic change of the PAC pattern between 803 K and 798 K. Above the M_S temperature the spectrum shape can be described by the frequency distribution around $\nu_Q = 0$ MHz characteristic for the probe in the cubic environment of B2 structure. The low temperature martensitic phase has the B19 structure of the lower symmetry. The *hfi* parameters determined at the room temperature showed that about 70% of the probe atoms exhibit the EFG described by the well-defined quadrupole frequency ν_Q = 48.8(7) MHz and asymmetry parameter η = 0.34(1), and the remaining probes have lower ν_Q = 37(2) MHz (η = 0.83(3)) with a slightly broader distribution width [Kul10]. These EFGs were attributed to the probe atoms substituting the Ti-2*f* and Pd-2*e* sites in the tetragonal B19 structure. Detailed information about the probe site occupation and the composition dependence on the observed EFGs was discussed in Chapter 3.1.

A similar temperature behavior of the PAC spectra, characteristic for the phase transition, was observed with the ^{181}Hf/^{181}Ta probe in TiPd doped with hafnium or zirconium. The evident transformation region allowed to determine the martensitic start temperature with a high accuracy. The M_S determined for pure TiPd implanted with ^{111}In and melted with 0.18 at.% ^{181}Hf reached 810(2) K and 778(2) K, respectively [Kul07,].

Composition influence on the martensitic transformation

In order to investigate the influence of impurities on the martensitic transformation in the TiPd alloy, a series of the PAC experiments were performed for the different concentrations of Hf, In and Zr. The samples were prepared with the different highest content of Hf, In and Zr admixtures However, no clear phase transformation was observed in the alloy doped with the maximum concentration of indium.

As can be seen in Figure 3.14, at 803 K a small fraction of sharp frequency characteristic for the martensite was already visible, where at 798 K still some fraction of the austenite remained. It means that the phase transformation takes place in a narrow temperature interval. The value of this interval increases with increasing amount of the third element. For the highest Hf concentration it reaches 20 K, and 40 K for only ~1 at.% Zr or In.

The martensitic start temperature M_S and the hysteresis loop width T_H established by PAC as a function of admixture content x are presented in Figure 3.15. The decrease of the starting temperature M_S with increasing impurity concentration was observed simultaneously with an increase of the hysteresis width T_H for all impurities used. It is worth noting that only for the

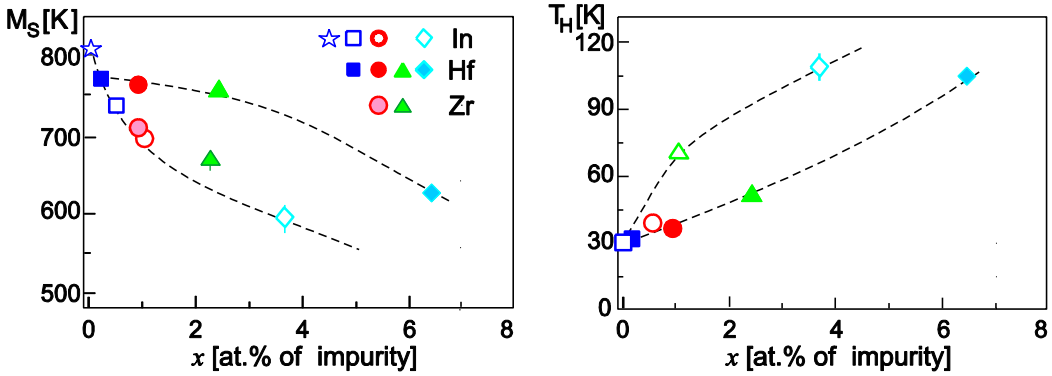

Fig. 3.15. Concentration dependence of the M_S and the T_H for the TiPd alloy with the indicated impurities Hf, Zr and In.

low admixture concentration a linear dependence was observed. The decrease of the M_S with an increasing amount of the third element was observed in the other SMA alloys, e.g. TiAu [Kaw06]. The linear relationship was observed up to the highest concentration 3 mol % of the admixture introduced into the TiAu alloy.

Table 3.4 summarizes the results obtained for the TiPd alloy with the impurity concentration around 1 at.%. The electron-atom ratio (*e/a*) value was calculated as a number of the sum of the outer electrons: *f*-, *d*- and *s*- for Hf; *d*- *s*- for Zr; and *d*-, *s*-, *p*- for In. The M_S increases with increasing number of the *e/a* calculated for $x \sim 1$ at.% of impurity. On the other hand, for the same element, the M_S value decreases with an increasing *e/a* number calculated for the rising content of Hf or In admixture [Kul10]. Comparison of the results obtained for Hf, In and Zr impurities confirmed that M_S depends on the concentration x as well as on the type of the admixture. Both M_S and T_H can be tuned by the proper amount of the suitable impurity. Although the effect of ternary element on the martensitic transformation has been reported for several SMAs, the origin of this phenomenon is still not fully understood. It is important that not only the alloy composition, but also the residual stress, internal stress or precipitates etc. could influence the M_S as well.

Table 3.4. Influence of the impurity and its concentration on the martensitic transformation parameters in the TiPd alloy.

impurity	concentr. x [at.%]	M_S [K]	T_H [K]	e/a	Ti:Pd
Hf	0.94	767(2)	36(3)	7.129	49:50 0.98
Zr	0.99	710(2)		7.043	48:51 0.95
In	1.04	700(2)	85(3)	7.029	50:49 1.02

Summary

This monograph presents the results of the selected experiments demonstrating the PAC as an important method to study fundamental topics of the hyperfine interaction in the condensed matter, as well as the advantages of its application in material sciences.

A comprehensive study of the Hf-Al and Zr-Al systems performed by our group has provided the important data about the quadrupole interaction in the intermetallic compounds. The detailed PAC measurements executed for the Hf-Al and Zr-Al phases, present in the phase diagrams, showed similarities between corresponding isostructural compounds. The series of experiments performed using two most common probes, ^{181}Ta and ^{111}Cd, gave the information about the localization of impurities in the host lattice. A high precision in the determination of the *hfi* parameters and their temperature dependencies allowed comparison with the theoretical values obtained by the DFT-based *ab initio* calculation. An interesting behavior of the probe in the intermetallic compounds have been discussed in details: the site preference (^{111}Cd or ^{181}Ta in (Hf/Zr/Ti)Al_3 compounds); the temperature-driven reversible switching between substitutional sites (^{111}Cd in ZrAg); the segregation into the phase admixture (^{111}Cd in ZrAl with minority Zr_2Al_3). The *hfi* parameters experimentally obtained by our group for different intermetallic systems such as Zr-Ag and Ti-Pd, as well as compounds with the $MoSi_2$ or C16 –type of structure built a very wide data-base used by many theoretical research groups for the EFG calculations. These results showed how important it is to understand the role of impurities in a compound at an atomic level.

The similarities between the Hf- and Zr- aluminides reflected the similar temperature dependence parameters. The quadrupole frequency followed mostly the linear or $T^{3/2}$ function. However, unusual relationships, such as an increase of the EFG with the temperature or an irregular dependence, were

also observed – e.g. Zr_3Al and Zr_2Al, which illustrated the very complicated problem of the EFG dependence on temperature.

To illustrate the sensitivity of the PAC method to the strength and orientation of the magnetic hyperfine field, I discussed the investigation of the texture and its changes in the thin Ni films upon heavy ion irradiation. I found that the compressive stress built up in the Ni layer during relaxation of the Xe-irradiated sample is responsible for the rotation of the B_{hf} direction by $\Delta\varphi=86(2)°$. The changes of B_{hf} orientation observed via PAC are consistent with the results obtained by MOKE.

The PAC experiments performed by me for the mechanically alloyed Fe-Mn powders provide the information about the extended composition region of the γ-Fe(Mn) phase. Moreover, the influence of the impurity concentration on the magnetic hyperfine field was proven. The number of foreign atoms in the nearest neighborhood of the probe atoms leads to the formation of the lower satellite B_{hf}.

A series of the PAC measurements with the ball milled $HfAl_2$, $HfAl_3$ and Hf_2Al_3 compounds were performed to study the influence of the grain boundaries on the EFG parameters. The distribution the width δ increases, while the fraction of the quadrupole frequency characteristic for the pure phase decreases with a decreasing grain size. The defects created in the crystal structure during the milling facilitated the recrystallization of the $HfAl_3$ sample to the low temperature phase. Moreover, the milling procedure followed by the annealing caused the decomposition of the initial Hf_2Al_3 phase into $HfAl_2$ and HfAl. The XRD analysis complemented the characteristic of the investigated nanopowders.

The sensitivity on the local environment of the PAC method was also illustrated by the case of the oxidation process observed in the zirconium aluminides. The results provided the oxidation resistance temperature of the measured compounds to be approximately 1073 K. The progressive formation of the stoichiometric ZrO_2 and Al_2O_3 and the growth of their agglomerations with increasing annealing temperature were observed. The assignment of the observed quadrupole frequencies to these oxides was confirmed by the calculations (computer code WIEN). Moreover, the experimentally obtained EFGs agreed with the calculated ones under assumption that the Ta probe is in a charged state.

The possibility to perform the PAC measurements in a very wide temperature region (from a few to several hundreds of K) makes it well-suited to follow phenomena as a function of temperature. The use of PAC in the phase transformation or phase analysis studies is one of its main application areas. As an example, I present study of the martensitic transformation in the

TiPd alloy doped with different impurities. The PAC measurements proved that the martensitic transformation parameters, M_S and T_H, can be tuned by the addition of a third element and the variation of its concentration. I found that the M_S temperature increased, while the T_H decreased with the increasing In, Hf or Zr content in TiPd, but the linear relationship was observed only for the low impurity concentration. Moreover, the slope of these relationships depends on the type of impurity used.

The presented applications of PAC in the condensed matter and material physics, showed one very important, but not the only possible, use of this hyperfine method. Many other applications not discussed here show the versatility of the problems that can be addressed with PAC. This method can be used to study the diffusion and other atomic movement in solids, surface, interface and grain boundaries, point defects identification and production, and exchange and dynamical interactions. The new digital spectrometers recently built by a few PAC groups, improved its functionality. A new class of scintillators based on the LYSO, $LaBr_3$ crystals strongly improved its sensitivity. The additional isotopes besides the most common ^{111}In/Cd and ^{181}Hf/Ta can be also adopted. This allows measurements of a new wide class of materials, including biological samples; something that was not possible until now.

Acknowledgements

This monograph is the result of many years of work and I could not have completed it without the support of many people. Let me devote this page to all who helped me.

First and foremost, I would like to thank Dr. hab. Paweł Wodniecki and Dr Barbara Wodniecka for all the years of our common work, support and the friendly atmosphere and stimulating discussions. I will always owe them debts of gratitude for all that they have done for me.

I would like to express my gratitude to Prof. K. P. Lieb and Dr M. Uhrmacher from the II Institute of Physics, University of Göttingen, for a fruitful collaboration and hospitality during my visits in Göttingen.

I wish to thank Prof. J. Styczeń and the heads of Department: Prof. U. Woźnicka and Assoc Prof. M. Marszałek, who have encouraged and motivated me to write this monograph.

Last but not least, great thanks to my colleagues from the IFJ PAN for vibrant discussions at the morning coffee meetings and for creating a friendly and motivating workplace.

References:

Ada94 J. M. Adams and G. L. Catchen, Phys. Rev. B 50 (1994) 1264.

Alo08 R. E. Alonso, L. A. Errico, E. L. Peltzer y Blancá, A. López-García, A. Svane, and N. E. Christensen, Phys. Rev. B 78 (2008) 165206.

And75 K. Andersen, Phys. Rev. B 12 (1975) 3060.

Aya94 A. Ayala, R. E. Alonso, and A. López-García, Phys. Rev. B 50 (1994) 3547.

Bar80 H. Barfuß, G. Böhnlein, H. Hohenstein, W. Kreische, M. Meinhold, H. Niedrig, Phys. Lett. A 79 (1980) 252.

Bel07 J. Beloševic-Čavor, V. Koteski, B. Cekič, A, Umicevič, Comp. Mater. Sci. 41 (2007) 164.

Bel08 J. Beloševic-Čavor, V. Koteski, B. Cekič, A, Umicevič, Comp. Mater. Sci. 43 (2008) 867.

Bel12 J. Beloševic-Čavor, V. Koteski, J. Radkovič, Solid State Commun. 152 (2012) 1072.

Ber69 R. Bèraud, I. Berkes, J. Danière, G. Marest, R. Rougny, Nucl. Instr. and Meth.69 (1969) 41.

Bla88 P. Blaha, K. Schwarz and P. H. Dederichs, Phys. Rev. B 37 (1988) 2790.

Bla01 P. Blaha, K. Schwarz, G. Madsen, D. Kvasnicka, and J. Luitz, "WIEN2k, an Aug-Plane Wave +Local Orbitals Program for Calculating Crystal Properties", K. Schwarz, Techn. Uni. Wien, 2001, (ISBN 3-9501031-1-2).

Bła09 A. Błachowski, U. D. Wdowik, K. Ruebenbauer, J. Alloy Compd. 485 (2009) 36.

But83 T. Butz, A. Lerf, Phys. Lett. A 97 (1983) 217.

Chr76 J. Christiansen, P Heubrs, R. Keitel, W Klinger, W. Loeffler, W. Sandner, and W. Witthuhn, Z. Phys. B 24 (1976) 177.

Col01 G. Collins and M. Zacate, Hyperfine Interact. 136/137 (2001) 641 and 647

Dar57 L. S. Darken and R. W. Gurry, "Physical Chemistry of Metals" New York: Mc Graw-Hill, 1957.

Dar12 G. N. Darriba, M. Renteria, H. M. Petrilli, and L. V. C. Assali, Phys. Rev. B86 (2012) 075203.

Don70 H. C. Donkersloot and J. H. N. van Vucht, J. Less-Common Met. 20 (1970) 83.

Eck76 K. H. Eckelmeyer, Scripta Metall. 10 (1976) 667.

Ena75 K. Enami, A. Nagasawa and S. Nenno, Scripta Metall. 9 (1975) 941.

Err02 L. A. Errico, G. Fabricius, M. Renteria, P. de la Presa, M. Forker, Phys. Rev. Lett. 89 (2002) 055503.

Err03 L. A. Errico, G. Fabricius, M. Renteria, Phys. Rev. B 67 (2003) 144104.

Err10 L. A. Errico, H. M. Petrilli, L. A. Terrazos, A. Kulińska, P. Wodniecki, K. P. Lieb, M. Uhrmacher, J. Belosevic-Cavor, and V. Koteski, *"Electric field gradients in ^{111}In-doped $(Hf/Zr)_3Al_2$ and $(Hf/Zr)_4Al_3$ mixed compounds: ab initio calculations, perturbed angular correlation measurements ad site preference"*, J. Phys: Condens. Mat. 22 (2010) 215501.

For08 M. Forker, P. de la Presa, W. Hoffbauer, S. Schlabach, M. Bruns, and D. V. Szabó, Phys. Rev. B 77 (2008) 054108.

Fra65 H. Fraunenfelder and R. M. Steffen, in Karlsson, E. Mathias and K. Siegbahn (eds.) Alfa-, Beta- and Gamma- Ray Spectroscopy, vol.2, North-Holland, Amsterdam, 1963, p.1118.

Her80 P. Herzog, K. Freitag, M. Reuschenbach, H. Walitzki, Z. Phys. A 294 (1980) 13.

Hoh64 P. Hohenberg, W. Kohn, Phys. Rev. B 136 (1964) 864.

Hoh77 H. Hohenemeser, A.R. Arends, H. de Waard, H.G. Devare, F. Pleiter and S. A. Drentje, Hyperfine Interact. 3 (1977) 297.

Hos96 H. Hosoda, K. Enami, A. Kamio, K. Inoue, J. Intel. Mat. Syst. Str. 7 (1996) 312.

Jae86 H. Jaeger, J. A. Gardner, J. C. Haygarth, and R. L. Rasera, J. Am. Ceram. Soc. 69 (1986) 458.

Jen76 P. Jena, Phys. Rev. Lett. 36 (1976) 418.

Kaj73 J. Kajfosz, Institute of Nuclear Physics (Cracow) Report No 858/PM, 1973.

Kan84 J. Kanamori, H. Akai, M. Akai, Hyperfine Interact. 17-19 (1984) 287.

Kaw06 T. Kawamura, R.Tachi, T. Inamura, H. Hosoda, K. Wakashima, K. Hamada, S. Miyazaki, Mat. Sci. Eng. A 438-440 (2006) 383.

Kes89 J. Kesten , Hyperfine Interact. 52 (1989) 17.

Koh65 W. Kohn, I.J. Sham, Phys. Rev. A 140 (1965) 1133.

Kul04 A. Kulińska, K. P. Lieb, G. A. Müller, M. Uhrmacher, and K. Zhang, "Magnetic texture in Ni films after Xe ion implantations measured with Perturbed Angular Correlation Spectroscopy", J. Magn. Magn. Mater. 272-276 (2004) 1149.

Kul06 A. Kulińska, B. Wodniecka, P. Wodniecki, *"The perturbed angular correlation studies of Ag-Zr compounds with ^{111}Cd probes"*, J. Alloy. Compd. 426 (2006) 76.

Kul07 A. Kulińska, P.Wodniecki, *"Martensitic transformation in TiPd shape memory alloys studied by PAC method with ^{181}Ta probes"*, Intermetallics 15 (2007) 1196.

Kul10 A. Kulińska, P.Wodniecki, M. Uhrmacher, *"Martensitic transformation in TiPd shape memory alloys studied by PAC method with ^{111}Cd probes"*, J. Alloy. Compd. 494 (2010) 17.

Kul10a A. Kulińska, P. Wodniecki, *"Electric field gradients in nanoparticles of $HfAl_2$ and $HfAl_3$ intermetallic compounds"*, Hyperfine Interact. 198 (2010) 47.

Kul12 A. Kulińska, H. M. Petrilli, L. Errico, V. Fernández, *"TDPAC and ab initio study of pure and ^{111}Cd- and ^{181}Ta-doped XAl_3 (X: Hf, Zr, Ti) intermetallics"*, Book of Abstract HFI/NQI Conference 2012, Pekin, China

Lin81 B. Lindgren, Y. K. Vijay, Hyperfine Interact. 9 (1981) 379.

Mad01 G.K.H. Madsen, P. Blaha, K. Schwarz, E. Sjöstedt, and L. Nordström, Phys. Rev. B 64 (2001) 195134.

Mül03 G. A. Müller, A. Kulińska, K. Zhang, R. Gupta, P. Schaaf, M. Uhrmacher and K. P. Lieb, *"MOMS and PAC studies of ion-irradiated ferromagnetic films"*, Hyperfine Interact. 151/152 (2003) 223.

Neu98 M. Neubauer, N. Reinecke, A. Kulińska, K. P. Lieb, M. Uhrmacher, P. Wodniecki,

M. Strömer, H. U. *Krebs " PAC measurements in laser deposited Ag/Fe and In/Fe alloys"*, J. Magn. Magn. Mater. 189 (1998) 8.

Nis78 K. Nishiyama, F. Dimmling and D. Riegel, Phys. Rev. Lett. 37 (1978) 357.

Rag75 R. S. Raghavan, E. N. Kaufmann and P. Raghavan, Phys. Rev. Lett. 34 (1975) 1280.

Rag76 P. Raghavan, E.N. Kaufmann, R. S. Raghavan, E. J. Ansaldo and R. A. Naumann, Phys. Rev. B 13 (1976) 2835.

Ren05 M. Rentería, G. N. Darriba, L. A. Errico, E. L. Muñoz, P. D. Eversheim, phys. status solidi b 242 (2005) 1928.

Sch96 G. Schatz and A. Weidinger, "*Nuclear Condensed Matter Physics: Nuclear Methods and Application",* Wiley, New York, 1996.

Sci85 A. Scian, E. Aglietti, M. C. Caracoche, P. C. Rivas, A. F. Pasquevich and A. López-García, J. Am. Ceram. Soc. 68 C (1985) 285.

Sjö00 E. Sjöstedt, L. Nordström, and D. J. Singh, Solid State Commun. 114 (2000) 15 see also S. Cottenier, *" Density Functional Theory and the Family of (L)APW-Methods: A Step-by-Step Introduction"* KU Leuven, Belgium, 2002 (http://www.wien2k.at/reg_user/textbooks).

Ste66 M. B. Stearns, Phys. Rev. 147 (1966) 439.

Ste72 R. M. Sternheimer, Phys. Rev. A 6 (1972) 1702.

Sur98 C. Suryanarayana, M. Grant Norton, "X-Ray Diffraction, A Practical Approach", Plenum, New York (1998).

Tay10 M.A. Taylor, R.E. Alonso, L.A. Errico, A. Lopez-Garcıa, P. de la Presa, A. Svane, and N.E. Christensen, Phys. Rev. B 82 (2010) 165203.

Tay12 M. A. Taylor, R. E. Alonso, L. A. Errico, A. Lopez-Garcıa, P. de la Presa, A. Svane, and N. E. Christensen, Phys. Rev. B 85 (2012) 155202.

Tch99 V. Tcherdyntsev, S. D. Kaloshkin, I. A. Tomilin, E. V. Shelekhov, and Y. V. Baldokhin, Z. Metallkd. 90 (1999) 747.

Tor06 D. Torumba, K. Parliński, M. Rots, and S. Cottenier, Phys. Rev. B 74 (2006) 144304.

Uhr01 M. Uhrmacher, A. Kulińska, Y. V. Baldokhin, V. V. Tcherdyntsev, S. D. Kaloshkin, A. Ponza, *"Hyperfine Study of Mechanically Alloyed Fe-Mn system"*, Hyperfine Interact. 136/137 (2001) 327.

Uhr02 M. Uhrmacher, A. Kulińska, Yu.V. Baldokhin, V. V. Tcherdyntsev, S.D. Kaloshkin, A. Maddalena, G. Principi, *"Fe-Mn Mechanically Alloyed powders characterized by local probes"*, Intermetallics 10 (2002) 571.

Vin73 I. Vincze, and I. A. Campbell, J. Phys. F 3 (1973) 647.

Wod01 P. Wodniecki, B. Wodniecka, A. Kulińska, M. Uhrmacher, K. P. Lieb, *"The Electric Field Gradients in (Zr/Hf)Al_3 and (Zr/Hf)$_2Al_3$ Intermetallic Compounds Studied by ^{181}Ta and ^{111}Cd-PAC spectroscopy"*, Hyperfine Interact. 136/137 (2001) 535.

Wod02 P. Wodniecki, B. Wodniecka, A. Kulińska, M. Uhrmacher, K. P. Lieb, *"The $HfAl_2$ and $ZrAl_2$ Laves phases studied by ^{181}Ta and ^{111}Cd perturbed angular correlation spectroscopy"*, J. Alloy. Compd. 335 (2002) 20.

Wod03 P. Wodniecki, B. Wodniecka, A. Kulińska, M. Uhrmacher, K. P. Lieb, *"Hf and Zr*

aluminides with B_f structure studied by PAC with ^{181}Ta and ^{111}Cd probes", J. Alloy. Compd. 351 (2003) 1.

Wod03a P. Wodniecki, B. Wodniecka, A. Kulińska, and A. Z. Hrynkiewicz, *"Oxidation of ZrAl and Zr_3Al compounds studied by ^{181}Ta PAC spectroscopy"*, Hyperfine Interact. 151/152 (2003) 291.

Wod03b P. Wodniecki, B. Wodniecka, A. Kulińska, *"ZrAg and Zr_2Ag phases studied by Perturbed angular correlation with ^{181}Ta probes"*, phys. status solidi b 236 (2003) 565.

Wod04 P. Wodniecki, B. Wodniecka, A. Kulińska, M. Uhrmacher, K.-P. Lieb, *"Zr_2Al and Zr_3Al compound studied by PAC with ^{181}Ta and ^{111}Cd probes"*, J. Alloy. Compd. 365 (2004) 52.

Wod05 P. Wodniecki, A. Kulińska, B. Wodniecka, M. Uhrmacher, K. P. Lieb, *"Hf_3Al_2 and Zr_3Al_2 isostructural aluminides studied by PAC with ^{181}Ta and ^{111}Cd probes"*, Hyperfine Interact. 158 (2005) 429.

Wod07 P. Wodniecki, A. Kulińska, B. Wodniecka, S. Cottenier, H. M. Petrilli, M. Uhrmacher and K. P. Lieb, *"Structural characterization of Zr_4Al_3 and Hf_4Al_3 compound by means of hyperfine interaction studies"*, Europhys. Lett. 77 (2007) 43001.

Wod09 P. Wodniecki, A. Kulińska, B. Wodnieck, J. Beloševic-Čavor, V. Koteski, *"Experimental and ab initio study of the electric field gradients at Ta and Cd impurities in $TiAl_3$"*, J. Alloy Compd. 479 (2009) 56.